A granular micromechanic-based model for Ultra High Performance Fiber-Reinforced Concrete (UHP FRC)

Luca Placidi ^a, Francesco dell'Isola ^{b,c,d,e}, Abdou Kandalaft ^f, Raimondo Luciano ^g, Carmelo Majorana ^h, Anil Misra ⁱ

- ^a International Telematic University Uninettuno, Italy
- b University of L'Aquila, Italy
- ^c International Research Center for the Mathematics and Mechanics of Complex Systems (M&MoCS), Italy
- d Warsaw University of Technology, Poland
- e CNRS Fellow, ENS, France
- f University of Catania, Italy
- g Parthenope University of Naples, Italy
- h University of Padua, Italy
- ⁱ Florida International University, United States of America

ARTICLE INFO

Keywords: Damage Plasticity Granular micromechanics Concrete Anisotropy

ABSTRACT

There is a growing interest in the application of UHP FRC (Ultra-High Performance Fiber-Reinforced Concrete) which has been under vigorous development since its inception over two decades ago. The advantages of these advanced materials is that they overcome the problems that plague conventional concrete, these include among others low residual strength and low tensile strength, poor crack control and resistance to crack propagation, which leads corrosion of the rebars and spalling. The aim of this paper is to provide a granular micromechanics-based model to describe the deformation behavior of UHP FRC material as it gives a robust method to link the micro-scale mechanisms with the macro-scale performance of materials with granular textures. In this model, the micro-scale is described by damage-elasto-plastic spring elements that represent the effective grain pair interactions decomposed into the so-called normal and tangential directions. Since the grain-pairs are variously oriented, the macro-scale response is obtained by integrating these interactions over the orientational space. Here we specialize the granular micromechanic model for UHP FRC by introducing a novel expression for the parameterized dissipation energy at the micro or the grain-pair scale. The newly introduced constitutive parameters are identified using experimental results for uniaxial extension and compression tests. The model is then applied to simulate the case of homogeneous compression, extension and shear to show the directional evolution of damage and plasticity and the consequent emergent anisotropy.

1. Introduction

Portland cement concrete is among the most utilized construction material widely used in structural applications as reinforced concrete in building and bridge construction among others (Contrafatto et al., 2012, 2016a,b; Scerrato et al., 2014). Conventional Portland cement concrete suffers from a range of limitations, including low tensile and residual strength, poor crack control and resistance to crack propagation, spalling and workability (Khoury et al., 2002; Schrefler et al., 2002a,b). Ultra-High-Performance Fiber-Reinforced Concrete (UHP FRC) is expected to overcome these limitations (Grimaldi and Luciano, 2000; Caporale et al., 2006). Many of the advantages and limitations of conventional Portland cement concrete can be traced

to the structure–property relationships at different scales (Fabbrocino and Farina, 2017; Giorgio et al., 2020a; Greco et al., 2017; Everstine and Pipkin, 1973; Hu et al., 1985; Turco et al., 2016) beginning from their chemical building blocks including minerals, such as calcium silicate/aluminate hydrates (Gawin et al., 1999, 2005a,b; Majorana et al., 1998; Dharmawardhana et al., 2014; Misra and Ching, 2013). A modeling approach based upon the atomistic scale is fraught with insurmountable challenges due to the complex composition, largely ill-defined atomic structures with substitutions and atomic defects, multi-scalar porosities, prohibitive computational expense and so on. In this case, a convenient point of departure, which can link the macroscale behavior in a practical way to the building blocks is through

Table 1
Concrete Mix design used in UHP FRC specimens

concrete imm design doed in orn Title specimens.							
Material	Cement	Fly Ash	Sand 8 mm	Water	Plasticizer	Fibers	
Dosage (kg/m³)	800	200	925	195	18	20	

the meso-scale of mineral agglomerates, or grains (Misra and Poorsolhjouy, 2015; Misra and Singh, 2015). To this end, the granular micromechanics approach (GMA) provides a paradigm for obtaining continuum models that link to effective grain interactions (Misra et al., 2021). The GMA has been particularly successful in developing micromacro linked models that predict a range of emergent phenomena, such as loading induced anisotropy evolution that could be caused by micro fracturing or microstructure changes under imposed conditions (Timofeev et al., 2021; Placidi et al., 2021), elastic chirality due to peculiar grain-pair elastic interactions (Giorgio et al., 2020b; Ciallella et al., 2023), emergent chirality due to directional evolution of damage (Timofeev et al., 2021) among many others. The elastic chiral behavior as well as the evolving chirality exhibited by such materials is in fact predictable only by considering generalized (higherorder or higher-gradient) continuum theories (Auffray et al., 2015b) that naturally arise through the application of GMA. The significance of higher-gradient or strain gradient theories have been discussed widely (Auffray et al., 2015a) and its application goes well beyond the regularization of computation for mesh independency (Ambati et al., 2015; Bourdin et al., 2000; Bourdin, 2007a,b; Bourdin et al., 2008; Del Piero et al., 2007; Francfort and Marigo, 1998; Li et al., 2016) to revelation of a range of hitherto unrecognized, latent or less understood phenomena such as chirality and size dependency of strain localization zones to micromechanisms (Abali et al., 2017; Placidi and Barchiesi, 2018). In order to accomplish such higher-gradient theories, variational methods (dell'Isola et al., 2000) are needed to properly establish the boundary conditions and the governing equations. Moreover novel computational techniques (Battista et al., 2016; Greco and Cuomo, 2013, 2014; Ramaglia et al., 2018) are also necessary for accomplishing numerical simulations correctly and accurately by changing the set of basis functions. Variational methods are important to develop proper models for metamaterials (dell'Isola et al., 2016, 2015; Fabbrocino and Carpentieri, 2017; Mancusi et al., 2017) and are able to consider not only conservative systems but also dissipative ones (Erden Yildizdag et al., 2023; Lancioni and Royer-Carfagni, 2009; Marigo, 1989; Reddy, 2011a,b) with the use of proper hemivariational generalization.

Here we apply the GMA, which we have previously applied to conventional cement concrete (Poorsolhjouy and Misra, 2017; Timofeev et al., 2021), to describe the behavior of UHP FRC. From the viewpoint of GMA, the key aspect that characterizes a particular material and in this case for example that distinguishes UHP FRC from the conventional cement concrete, is the micro-scale elastic and dissipation behavior represented by the effective grain-pair interactions decomposed into the so-called normal and tangential directions. Dissipation phenomena has been widely discussed in continuum mechanics (Aifantis, 1984, 1987, 1992) from macro-scale as well as micro-scale viewpoints (Scerrato et al., 2015; Altenbach and Eremeyev, 2008; Giorgio et al., 2016, 2017). Dissipation due to material irrecoverable damage or plastic deformations in materials such as UHP FRC can take place through a variety of interacting mechanisms at structural scales ranging from the atomic through many intervening structures, such as grain boundaries and interphases, to those scales at which we consider continuum models. At each scale, there are a myriad of mechanisms that interact to produce damage and plasticity related dissipation in relation to the applied boundary actions. In GMA, this complex of dissipation mechanism is described through the effective grain-pair interactions as the representative of all the myriad lower scale mechanisms. In a material with random isotropic microstructure, the effective grainpair are considered to be equally likely oriented in all directions and the macro-scale (or continuum material point) response obtained by integrating these interactions over the orientational space. We remark

that the microstructural features that may be included or emphasized depend upon the modeling approach. In GMA methodology elaborated in this work, the orientation of the effective grain-pair is the key microstructural feature that appears in the model. As we have described, the effective grain-pair is conceived to represent the elastic-storage and dissipation phenomenology in given orientations. In this sense, the continuum model can be devised to describe various inherent anisotropies in its reference (or unloaded) state. Moreover, it is notable that during prescribed boundary actions, the deformation suffered by a continuum material point results in the various grain-pair directions experiencing different loading histories resulting in directional evolution of damage and plasticity and an overall evolving macro-scale anisotropy.

The structure of this paper is as follows. In Section 2 we report the basic experimental characteristics of UHP FRC, some of which we aim to model in the paper. In Section 3 we recap the granular micromechanic approach we use in the rest of the paper. The formulation is here synthetic and reduced for the specific homogeneous case that is investigated with the used simplified boundary conditions of Figs. 4 and 6. As a consequence, we avoid the derivation of strain gradient regularization terms in the elastic energy in Section 3.1, already presented in other publications, but we present a novel form of the dissipation energy in Section 3.2 that is able not only to (i) provide asymptotically and exponentially, in (36)-(37), the failure mechanism, but also to (ii) consider a predefined threshold (in tension and in compression according to (21)) to activate not only plastic, see e.g. (38)-(39), but also damage, see e.g. (36)-(37), phenomena. In Section 4 we expose the used methodologies for the numerical characterization of those parameters introduced in the energy functional reported in (22) to serve the experimental data of Sections 2.3 and 2.4. In Section 5 we present the promised numerical simulations. To do this, we define the investigated cases in Sections 5.1 and 5.2 and show the simulations in Section 5.3 with the numerical method in Section 5.3. Conclusions and outlook end the paper in Section 6.

2. Experimental results of UHP FRC

2.1. The mix design of the material

Mechanical properties of concrete are determined by the concrete mix design that consists of the dosage of each composing material, that is the proportions of cement, aggregates, additives, and water. The concrete mix design for the UHP FRC modeled and simulated in this paper has been developed in earlier works (Abdou et al., 2022). Using this mix proportion, test samples were fabricated using a UHP FRC mix that is self-consolidating. The key for producing this type of concrete is the choice of mean equivalent aggregate diameter, defined as the mean of all the aggregates based on the 500 g sample classified through sieve analysis. Lower equivalent diameter of the aggregates results in better performance in terms of flowability and viscosity of fresh concrete. For the UHP FRC mix, 8 mm equivalent diameter aggregates were used. In addition, by substituting a significant amount of Portland cement with pozzolans such as fly ash, silica fume or others, along with the fibers either made of PP material (polypropylene) or steel, helps in achieving higher compressive strengths (Bragaglia et al., 2021a,b; D'Ambra et al., 2019; Grande et al., 2020). The concrete mix of the samples modeled in this paper include the PP fibers and a substitution of part of the cement dosage by fly ash. The fibers are expected to play an important role in the strength of post crack stage, when the concrete cracks and the fibers (i) hold the concrete element together and (ii) prevent the opening of the crack any further. The post cracking effectiveness of

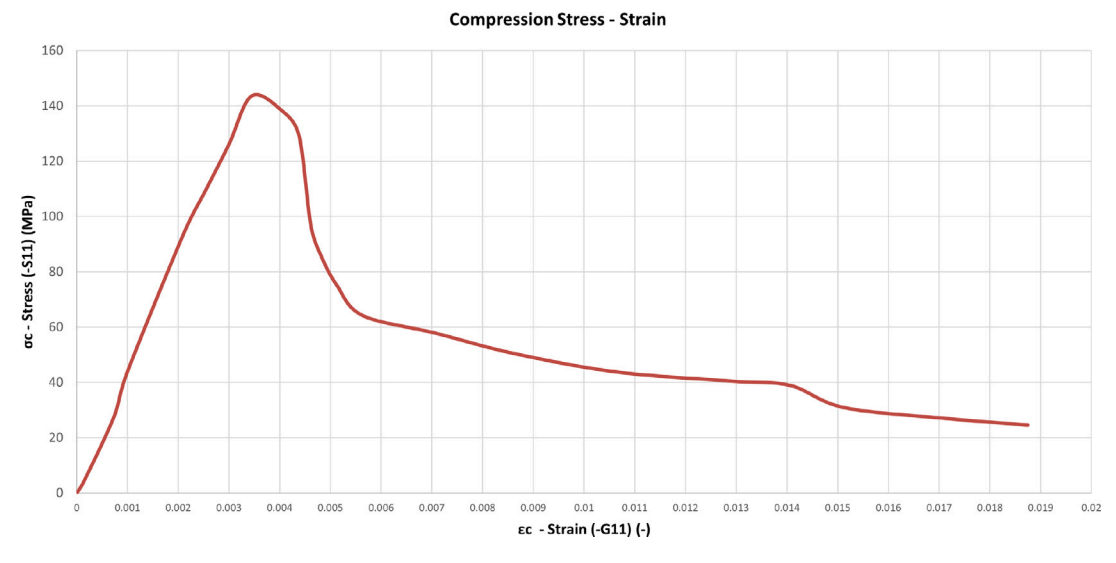


Fig. 1. UHP FRC Compressive Experimental Test Results According to the EN 12390 standard (Stress $\sigma_c = -S_{11}^{3D}$ - Strain $\varepsilon_c = -G_{11}$ Graph). Average (over 3 samples) response is shown, with a variance percentage of 10.

Table 2
Polypropylene Fibers' Properties

rotypropytene ribers rroperties.		
Length (mm)	55	
Equivalent Diameter (mm)	0.8	
Density (Kg/m³)	910	
Tensile strength (MPa)	560	
Elastic Modulus (MPa)	3900	
Shape	Crimped	
Melting Point (C°)	160	

fibers in UHP FRC are measured with both the residual strength and the tensile strength (Abdou et al., 2022).

The following tables 1 and 2 give the concrete mix design dosages and the properties of the polypropylene (PP) fibers used in the tests, respectively.

2.2. General aspects of the experimental tests

UHP FRC has a high compressive strength at 28 days (see Section 2.3). Other characterizations are done with the direct tensile (see Section 2.4) and three point loading tests according to EN 14651 (UNI/CT 021/SC 04 UNI/CT 021, UNI/CT 021/GL 03, 2015). The latter is important because it gives the understanding of the behavior of the fibers after the first crack in the concrete by insertion of an initial notch in the middle of the lower side to govern the path of the crack. In this test a displacement is applied in the upper middle part and both force and CMOD (Crack Mouth Opening Displacement) are recorded. The fibers prevent the failure of the structural element and limit the crack opening in the sample. They also result in strength hardening or softening. To focus the present work to homogeneous deformation cases, we will consider the simulation of the three point bending test in a future publication.

2.3. Compressive test

The compressive strength has been executed according to the EN 12390 (UNI/CT 009, 2022) standard where 3 samples of the concrete mix have been cast in Abdou et al. (2022). Thus, they have performed the tests with the results shown in Fig. 1, where we report the average (over the 3 mentioned specimens) compressive stress vs the average compressive strain with a variance percentage of 10. Each side of the cubic specimens is A = 100 mm and the stress is calculated by dividing the applied force by the surface area of the cube face.

From Fig. 1 the experiment starts with a linear elastic stage,

$$-S_{11}^{3D} = \sigma_c = E_c \varepsilon_c = -E_c G_{11},\tag{1}$$

where the compressive stress σ_c is identified with the opposite of the component S_{11}^{3D} of the stress tensor in a 3D model, ϵ_c is the compressive strain, that is identified with the opposite of the component G_{11} of the strain tensor (properly defined in (10)) and with an initial modulus of elasticity in compression that can be easily extrapolated,

$$E_c \cong 45.55 \text{ GPa} \tag{2}$$

At the end of this stage, the peak is reached. It defines the compressive strength of the tested concrete which, in this case, is around

$$\sigma_c^{\text{max}} = 143 \text{ MPa}.$$

Beyond the first elastic stage, a softening one occurs. A normal traditional non fiber reinforced concrete would undergo an instant failure and the test would terminate at this point. However, this is not the case with the UHP FRC because of the presence of the fibers. In fact, beyond the peak, a plateau starts where the fibers intervene in the deformation process preventing a sudden failure. The material response is a gradual softening with non negligible resisting force with higher strains.

2.4. Direct tensile test

With regards to the direct tensile test using a *dog-bone* specimen, the dimensions of the sample in the neck area are 200 mm long with a cross section of $150 \text{ mm} \times 80 \text{ mm}$ as shown in Fig. 2. The choice of relatively larger cross-section ensures sampling of sufficient randomly oriented fibers to permit correct evaluation of the effect of fibers on the tensile performance. Fig. 3 expresses the curve of the averaged (over the 3 samples that were experimentally tested) tensile stress, with a variance percentage of 12, vs the average tensile strain. Even for the tensile case we have an initial linear elastic behavior

$$S_{11}^{3D} = \sigma_t = E_t \varepsilon_t = E_t G_{11}, \tag{3}$$

where the tensile stress σ_t is identified with the component S_{11}^{3D} of the stress tensor in a 3D model, ε_t is the tensile strain, that is identified with the component G_{11} of the strain tensor (properly defined in (10)) and the modulus of elasticity in tension is

$$E_t \cong 21.5 \text{ GPa.}$$
 (4)

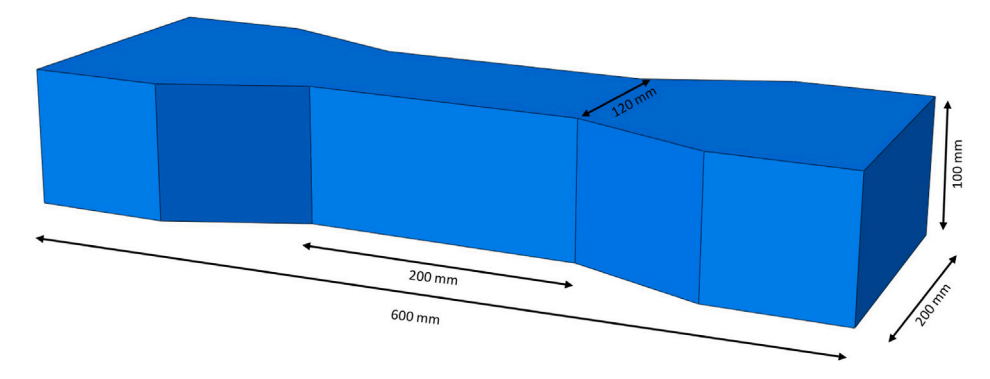


Fig. 2. UHP FRC Tensile Test (Dog Bone) Specimen's Dimensions.

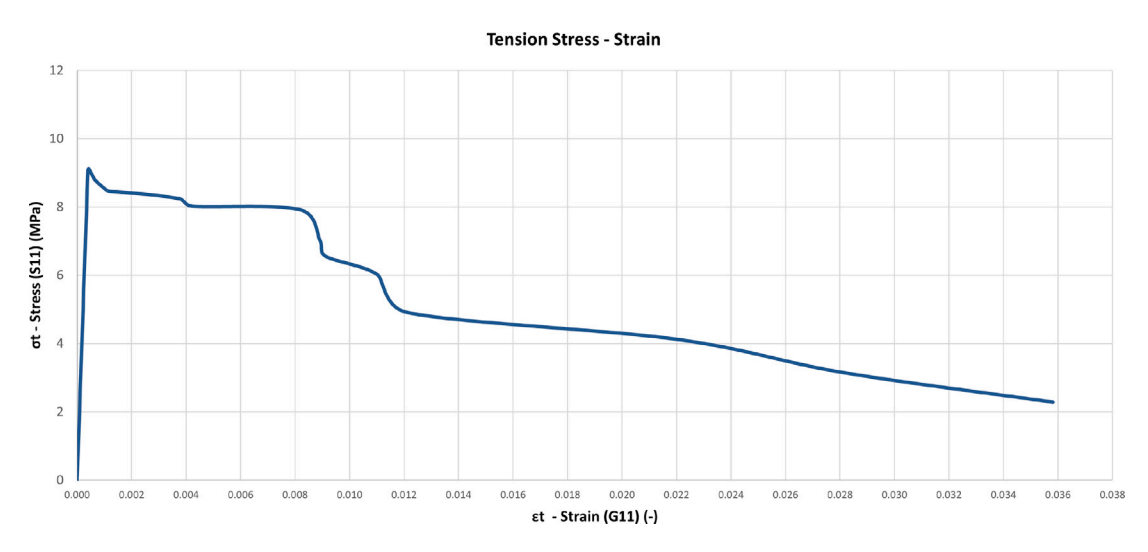


Fig. 3. UHP FRC Direct Tensile Experimental Test Results (Stress $S_{11}^{3D} = \sigma_i$ - Strain $\varepsilon_i = G_{11}$ Graph). Average (over 3 samples) response is shown, with a variance percentage of 12.

The linear elastic part is defined from the beginning to the peak, where the ultimate tensile strength is measured,

$$\sigma_t^{\text{max}} \cong 9.12 \text{ MPa.}$$

This value is much higher than any other normal concrete, e.g., for the C25 case, which is one of the most commonly used concrete, the tensile strength is typically 2.6 MPa. A normal non fiber reinforced concrete would fail and the sample would break right after reaching the peak. In the case of UHP FRC it can be seen that the sample starts to undergo softening stage after the peak. Experimental tests performed with different mix design have shown that the higher the dosage of the fibers, the larger is the plateau after the peak. The sudden stress drop events as extension progresses are likely due to the fiber–matrix debonding and even fiber breaking. In any case the overall post peak response is one of steady softening rather than catastrophic fracture due to the resisting mechanism provided by the fibers.

Additional observations on the tests could be made as follows:

- (a) The elastic stiffness is consistent in both tension and compression test results, reflecting, in this stage, a similar but not identical behavior.
- (b) The discrepancy between tension and compression test outcomes is attributed to the material's damage-plastic behavior. Notably, the material exhibits distinct responses in the damage-plastic phase, wherein fibers perform optimally under tension. This explains why the compression test does not show a significant increase in ultimate strength but rather an improvement in sustaining resistance until failure.

- (c) A stress–strain plateau is consistently observed just before failure in each presented test. This phenomenon is attributed to the reinforcing characteristics of fibers in concrete, allowing for increased deformations at higher stress levels until eventual failure of the element.
- (d) All the aforementioned factors have been carefully considered in the model and subsequent simulation to ensure the most accurate representation of the data.

3. Homogenization recap within the framework of granular micromechanics

3.1. The elastic strain energy density

In this continuum formulation, and for a given point X of the continuum body \mathcal{B} , we assume a damage-elasto-plastic pair interaction for each orientation, that we denote by the unit vector \hat{c} . The elastic energy that we associate to each pair-interaction, according to the same homogenization procedure adopted by Cauchy (Cauchy, 1828) and Navier (Navier, 1827) almost 2 hundreds years ago, is therefore integrated over all the orientations \hat{c} , i.e. over the unit circle \mathcal{S}^1 in the present 2D case, in order to obtain the elastic energy U per unit area, i.e. the elastic strain energy density. Besides, the elastic energy associated to each orientation is assumed to be quadratic with respect to two relative displacements, i.e. the normal displacement u_η and the tangential displacement u_τ , that we will define in (8) and (9), respectively, as a function not only of the average distance L, but also

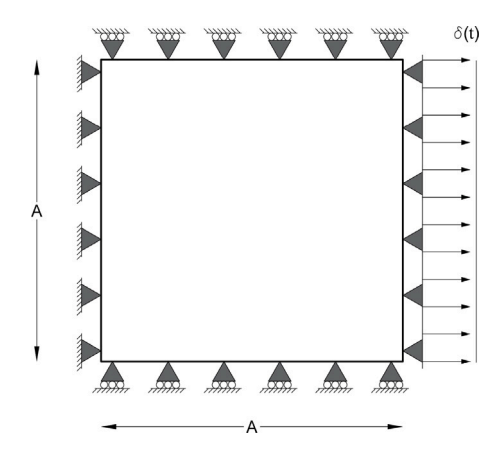


Fig. 4. Tension (with $\delta(t) > 0$)/compression (with $\delta(t) < 0$) boundary conditions for a squared shape body $\mathcal B$ inducing homogeneous deformation reported in (68).

of the orientation \hat{c} and of the Green–Saint-Venant strain tensor G. The pair-interaction elastic energy is also proportional to the damage normal stiffness $k_{\eta,D}$ and to the damage tangent stiffness $k_{\tau,D}$, that are reduced by the normal damage D_{η} and by the tangent damage D_{τ} . These stiffness and damage variables are all functions not only of the point X of the continuum body B but also of the orientation \hat{c} of the unit circle S^1 . In formulae we have that the elastic strain energy density U is defined as follows,

$$U = \int_{SL} \left[\frac{1}{2} k_{\eta, D} \left(u_{\eta}^{el} \right)^2 + \frac{1}{2} k_{\tau, D} \left(u_{\tau}^2 \right) \right] dA, \quad \forall X \in \mathcal{B}$$
 (5)

where dA is the area element on the unit circle S^1 , the elastic part u_η^{el} of the normal displacement u_η is postulated to be equal to the difference between the normal displacement u_η and its plastic part u_η^{pl} ,

$$u_{..}^{el} = u_{..} - u_{..}^{pl}, \tag{6}$$

where the normal plastic displacement u_{η}^{pl} is assumed to be the difference between two plastic multipliers, the accumulation plastic tension λ_n^t and the accumulation plastic compression λ_n^c ,

$$u_n^{pl} = \lambda_n^t - \lambda_n^c. \tag{7}$$

According to the definitions in Placidi et al. (2021), Timofeev et al. (2021), normal and squared tangential displacements are defined as follows,

$$u_n = LG_{ij}\hat{c}_i\hat{c}_j \tag{8}$$

$$u_{\tau}^2 = 4L^2 G_{ij} G_{ab} \left(\delta_{ia} \hat{c}_j \hat{c}_b - \hat{c}_i \hat{c}_j \hat{c}_a \hat{c}_b \right) \tag{9}$$

where, as it was stated at the beginning of this Section, the unit vector \hat{c} is the direction of the considered pair interaction and it belongs to the domain S^1 , that is the unit circle over which the integral in (5) is computed; the Green–Saint-Venant tensor G is a tensor of 2nd order,

$$G = \frac{1}{2} \left(F^T F - I \right), \tag{10}$$

where F is the deformation gradient,

$$F = \nabla \chi, \tag{11}$$

that is defined in terms of the placement function $\chi(X,t)$, that is a function of the position X and of the time t. The damage variables D_{η} and D_{τ} have the role to reduce the non-damage normal stiffness k_{η} and the non-damage tangent stiffness k_{τ} , respectively,

$$k_{n,D} = k_n (1 - D_n), \qquad k_{\tau,D} = k_\tau (1 - D_\tau).$$
 (12)

Besides, non-damage normal stiffness k_{η} in tension k_{η}^t and in compression k_{η}^c is different in granular materials in general and this is true also

for UHP FRC. The presence of two different stiffness (i.e. the normal and the tangential stiffness) implies the need for two different damage variables since the normal and tangential damage may be expected to evolve differently. We consider a certain orientation \hat{c} to be in tension or in compression on the basis of the sign of the elastic part u_{η}^{el} of the normal displacement u_{η} . Thus,

$$k_{\eta} = k_{\eta}^{t} \Theta\left(u_{\eta}^{el}\right) + k_{\eta}^{c} \Theta\left(-u_{\eta}^{el}\right), \tag{13}$$

where $\Theta(x)$ is the Heaviside function, that is equal to unity value if $x \ge 0$ and to zero if x < 0. Insertion of (6), (8), (9) and (12) into (5) yields the elastic energy per unit area in a more compact form,

$$U = \frac{1}{2} \mathbb{C}_{ijab} G_{ij} G_{ab} + \mathbb{P}_{ij} G_{ij}, \tag{14}$$

where, accounting for the symmetrization induced by the symmetry of the strain tensor G, the elastic stiffnesses \mathbb{C} , and the pre-stress \mathbb{P} are identified as follows

$$\mathbb{C}_{ijab} = L^2 \int_{\mathbb{S}^1} k_{\eta} \left(1 - D_{\eta} \right) \hat{c}_i \hat{c}_j \hat{c}_a \hat{c}_b dA \tag{15}$$

$$+L^{2}\int_{c_{1}}k_{\tau}\left(1-D_{\tau}\right)\left(\left(\delta_{ia}\hat{c}_{j}\hat{c}_{b}+\delta_{ib}\hat{c}_{j}\hat{c}_{a}+\delta_{ja}\hat{c}_{i}\hat{c}_{b}+\delta_{jb}\hat{c}_{i}\hat{c}_{a}\right)-4\hat{c}_{i}\hat{c}_{j}\hat{c}_{a}\hat{c}_{b}\right)dA$$

$$\mathbb{P}_{ij} = -L \int_{\mathbb{S}^1} k_{\eta} \left(1 - D_{\eta} \right) u_{\eta}^{pl} \hat{c}_i \hat{c}_j dA \tag{16}$$

According to the legacy of the continuum mechanics (Auffray et al., 2015a), a consequence of the expression (14) for the elastic energy per unit area is the form of the stress tensor S, i.e.,

$$S_{ij} = \frac{\partial U}{\partial G_{ii}} = \mathbb{P}_{ij} + \mathbb{C}_{ijab}G_{ab} \tag{17}$$

where the pre-stress $\mathbb P$ is therefore interpreted as the stress S with no strain, i.e. with G=0. We oversee that (i) the normal plastic displacement u_η^{pl} has a direct influence, as expected, from (16) on the pre-stress and (ii) damage variables D_η and D_τ have a direct influence from (15) on the stiffness tensor.

3.2. The dissipation energy density

Damage and plastic variables are dissipative in nature and their evolution is related to the form of the dissipation energy. Similarly to what was done for the elastic energy density in (5) we assume a form for the dissipation for a given pair orientation \hat{c} and then we integrate such a dissipation over the unit circle S^1 ,

$$W = \int_{S^{1}} \left\{ \frac{1}{2} B^{2} \left[k_{\eta} g \left(D_{\eta}, D_{mtr} \right) + k_{\tau} g \left(D_{\tau}, D_{mtr} \right) \right] + \left(1 - D_{\eta} \right) \left(\sigma_{\eta}^{t} \lambda_{\eta}^{t} + \sigma_{\eta}^{c} \lambda_{\eta}^{c} \right) \right\} dA, \quad \forall X \in \mathcal{B}$$

$$(18)$$

where B is the initial characteristic damage displacement, σ_{η}^{t} and σ_{η}^{c} are the initial plastic yielding points in tension and in compression, respectively, and the function g is defined as follows,

$$g(d, d_{mtr}) = 2 - 2\log(1 - d_{mtr}) + (\log(1 - d_{mtr}))^{2} + (d - 1)(2 - 2\log[(1 - d_{mtr})(1 - d)] + (\log[(1 - d_{mtr})(1 - d)])^{2}).$$

It is worth to note that its derivative with respect to the first variable *d* takes a simplified form,

$$\frac{\partial g}{\partial d} = \left[\log \left(1 - d_{mtr} \right) (1 - d) \right]^2 \tag{19}$$

and that with d = 0, we have

$$g\left(0, d_{mtr}\right) = 0. (20)$$

The variable D_{mir} has different values, i.e. D_c^{mir} and D_t^{mir} , in compression and in tension, respectively,

$$D_{mtr} = D_c^{mtr} \Theta\left(-u_{\eta} + \lambda_{\eta}^t - \lambda_{\eta}^c\right) + D_t^{mtr} \Theta\left(u_{\eta} - \lambda_{\eta}^t + \lambda_{\eta}^c\right), \tag{21}$$

where a direction \hat{c} is assumed to be in compression or in tension looking for the sign, negative or positive, respectively, of the elastic part u_{ν}^{el} of the normal displacement according to (6).

It is worth to give an interpretation of the form (18) of the dissipation energy. The second addend involves normal damage and plastic descriptors. It is linear with respect to plastic descriptors and the coefficients of such a linearity will be interpreted as a yielding threshold once the corresponding KKT will be derived. It is possible to prove that the dependence of such coefficients with normal damage makes the activation of plastic evolution to be independent with respect to damage. Thus, the dissipation increases indefinitely with plastic descriptors but the damage factor attenuate such a tendency. The first addend is more complicated. It involves only damage. First of all the restriction (20) makes the dissipation to be null with damage equal to zero and the positiveness of (19) makes the dissipation monotonic with damage. Besides, the higher the value of the parameter d_{mtr} the higher the value of the derivative (19) and therefore the higher is the difficulty for the material to increase the level of damage. Besides, we will achieve a clear interpretation of the variables D_c^{mtr} and D_t^{mtr} introduced in (21) after the exploitation of the Hemivariational principle in the following Section 3.3. It is worth to note finally that the first addend of (18) has been split into two parts, one for normal and one for tangent components.

3.3. The hemivariational principle for the continuum model

The (action) energy functional is defined as the sum of the elastic and dissipation energies,

$$\mathcal{E}\left(\chi, D_{\eta}, D_{\tau}, \lambda_{\eta}^{t}, \lambda_{\eta}^{c}\right) = \int_{\mathcal{B}} \left[U + W - b_{i}^{ext} \chi_{i}\right] dV - \int_{\partial_{\tau} \mathcal{B}} \left[t_{i}^{ext} \chi_{i}\right] dV, \quad (22)$$

integrated over the 2D reference configuration \mathcal{B} . b^{ext} is the external distributed body force acting on the surface \mathcal{B} and t^{ext} is the external distributed force acting on those part $\partial_N \mathcal{B}$ of the boundary $\partial \mathcal{B}$ for which we do not prescribe the placement χ (i.e., we do not prescribe Dirichlet boundary conditions) and therefore on which we prescribe Neumann boundary conditions. The energy functional \mathcal{E} is a functional of the fundamental kinematical descriptors of the model, i.e. the placement

$$\chi(\boldsymbol{X},t),\tag{23}$$

that is a function of the position X and of the time t, and the 4 irreversible descriptors

$$D_n(X, \hat{c}, t), D_{\tau}(X, \hat{c}, t), \lambda_n^t(X, \hat{c}, t), \lambda_n^c(X, \hat{c}, t),$$
 (24)

that are all functions not only of the position X and of the time t but also of the orientation \hat{c} . Damage $(D_{\eta} \text{ and } D_{\tau})$ and plastic $(\lambda_{\eta}^{t} \text{ and } \lambda_{\eta}^{c})$ variables are defined as non-decreasing in time. Thus, these inequality assumptions.

$$\frac{\partial D_{\eta}}{\partial t} \geq 0, \quad \frac{\partial D_{\tau}}{\partial t} \geq 0, \quad \frac{\partial \lambda_{\eta}^{t}}{\partial t} \geq 0, \quad \frac{\partial \lambda_{\eta}^{c}}{\partial t} \geq 0, \quad \forall X \in \mathcal{B}, \quad \forall \hat{c} \in S^{1}, \quad (25)$$

imply a generalization of standard variational principle into a so-called hemivariational principle. To do this, let us introduce a monotonously increasing time sequence $T_i \in \left\{T_i\right\}_{i=0,\dots,M}$ with $T_i \in \mathbb{R}$ and $M \in \mathbb{N}$ and give initial datum on each of the fundamental kinematic quantities for i=0, i.e., for time $t=T_0$. A family of placements χ defines the motion for each time $t=T_0,T_1,\dots,T_M$. The set AM_t of kinematically admissible placements is defined for a given time t and the set AV_t is defined as the corresponding space of kinematically admissible variations, i.e., $v=\delta\chi\in AV_t$. Admissible variations β of the irreversible kinematic quantities $\left(D_{\eta},D_{\tau},\lambda_{\eta}^t,\lambda_{\eta}^c\right)$ must be positive because of (25), namely

$$\beta = \left\{ \delta D_{\eta}, \delta D_{\tau}, \delta \lambda_{\eta}^{t}, \delta \lambda_{\eta}^{c} \right\} \in \mathbb{R}^{+} \times \mathbb{R}^{+} \times \mathbb{R}^{+} \times \mathbb{R}^{+}. \tag{26}$$

By definition, the first variation $\delta \mathcal{E}$ of the energy functional (22) is calculated as

$$\delta \mathcal{E} = \mathcal{E} \left(\chi + \delta \chi, D_{\eta} + \delta D_{\eta}, D_{\tau} + \delta D_{\tau}, \lambda_{\eta}^{t} + \delta \lambda_{\eta}^{t}, \lambda_{\eta}^{c} + \delta \lambda_{\eta}^{c} \right) - \mathcal{E} \left(\chi, D_{\eta}, D_{\tau}, \lambda_{\eta}^{t}, \lambda_{\eta}^{c} \right). \tag{27}$$

Besides, the increment of (23)–(24), i.e. of the fundamental kinematic quantities, at $t = T_i$ is given by the difference between these quantities as evaluated at times $t = T_i$ and $t = T_{i-1}$, namely

$$\left(\Delta\chi,\Delta D_{\eta},\Delta D_{\tau},\Delta\lambda_{\eta}^{t},\Delta\lambda_{\eta}^{c}\right)_{T}=\left(\chi,D_{\eta},D_{\tau},\lambda_{\eta}^{t},\lambda_{\eta}^{c}\right)_{T}-\left(\chi,D_{\eta},D_{\tau},\lambda_{\eta}^{t},\lambda_{\eta}^{c}\right)_{T}.$$

The same definition is utilized for the increment $\Delta \mathcal{E}$ of the energy functional

$$\Delta \mathcal{E} = \mathcal{E}\left(\chi + \Delta \chi, D_{\eta} + \Delta D_{\eta}, D_{\tau} + \Delta D_{\tau}, \lambda_{\eta}^{t} + \Delta \lambda_{\eta}^{t}, \lambda_{\eta}^{c} + \Delta \lambda_{\eta}^{c}\right) - \mathcal{E}\left(\chi, D_{\eta}, D_{\tau}, \lambda_{\eta}^{t}, \lambda_{\eta}^{c}\right). \tag{28}$$

Finally, as a matter of fact, the hemi-variational principle is formulated as follows

$$\Delta \mathcal{E} \geq \delta \mathcal{E} \quad \forall v = \delta \chi \in AV_t, \qquad \forall \beta = \left(\delta D_{\eta}, \delta D_{\tau}, \delta \lambda_{\eta}^t, \delta \lambda_{\eta}^c\right) \in \mathbb{R}^+ \times \mathbb{R}^+ \times \mathbb{R}^+ \times \mathbb{R}^+.$$
(29)

As remarked in Marigo (1989), the inequality (29) states that the actual energy release rate, proportional to $\Delta \mathcal{E}$, is not lower than any possible one. Thus, it constitutes a kind of principle of maximum energy release rate.

3.4. The Euler Lagrange equations for the continuum model

The derivation of the Euler Lagrange equations is done according to the derivation deduced in Placidi et al. (2022, 2021), Timofeev et al. (2021). First of all, the reversibility of the admissible placement variation $v = \delta \chi \in AV$, implies the following variational equality,

$$\mathcal{E}\left(\chi + \delta\chi, D_{\eta}, D_{\tau}, \lambda_{\eta}^{t}, \lambda_{\eta}^{c}\right) - \mathcal{E}\left(\chi, D_{\eta}, D_{\tau}, \lambda_{\eta}^{t}, \lambda_{\eta}^{c}\right) = \frac{\partial \mathcal{E}}{\partial \chi} \delta\chi = 0,$$

$$\forall v = \delta\chi \in AV_{t},$$
(30)

that corresponds to those Partial Differential Equations (PDEs) and Boundary Conditions (BCs) valid for standard geometrically nonlinear elastic materials for fixed values of irreversible kinematic quantities $\left(D_{\eta}, D_{\tau}, \lambda_{\eta}^{t}, \lambda_{\eta}^{c}\right)$,

$$S_{ii,i} + b_i = 0, \quad \forall X \in \mathcal{B}, \quad S_{ii} n_i = t_i, \quad \forall X \in \partial_N \mathcal{B}.$$
 (31)

Secondly, following the methods developed in the same papers in Placidi et al. (2022, 2021), Timofeev et al. (2021), Misra et al. (2021), the variational inequality (29) implies the following KKT conditions corresponding to the 4 irreversible kinematic descriptors $(D_{\eta}, D_{\tau}, \lambda_{\eta}^{t}, \lambda_{\eta}^{c})$,

$$\left\{ D_{\eta} - \tilde{D}_{\eta}(u_{\eta}, \lambda_{\eta}^{t}, \lambda_{\eta}^{c}) \right\} \Delta D_{\eta} = 0, \tag{32}$$

$$\left\{D_{\tau} - \tilde{D}_{\tau}(u_{\tau}, \lambda_{\eta}^{t}, \lambda_{\eta}^{c})\right\} \Delta D_{\tau} = 0, \tag{33}$$

$$\left\{\lambda_n^t - \tilde{\lambda}_n^t(u_n, \lambda_n^c, D_n)\right\} \Delta \lambda_n^t = 0, \tag{34}$$

$$\left\{\lambda_{\eta}^{c} - \tilde{\lambda}_{\eta}^{c}(u_{\eta}, \lambda_{\eta}^{t}, D_{\eta})\right\} \Delta \lambda_{\eta}^{c} = 0, \tag{35}$$

where the thresholds are evaluated by derivation of the energy functional (22) and reported here,

$$\tilde{D}_{\eta}(u_{\eta}, \lambda_{\eta}^{t}, \lambda_{\eta}^{c}) = 1 - \frac{1}{1 - D_{mtr}} \exp\left(-\frac{\sqrt{2\frac{\sigma_{\eta}^{t} \lambda_{\eta}^{t} + \sigma_{\eta}^{c} \lambda_{\eta}^{c}}{k_{\eta}} + \left(u_{\eta} - \lambda_{\eta}^{t} + \lambda_{\eta}^{c}\right)^{2}}}{B}\right) (36)$$

$$\tilde{D}_{\tau}(u_{\tau}, \lambda_{\eta}^{t}, \lambda_{\eta}^{c}) = 1 - \frac{1}{1 - D_{mtr}} \exp\left(-\frac{\sqrt{\left(u_{\tau}\right)^{2}}}{B}\right),\tag{37}$$

$$\tilde{\lambda}_t(u_\eta, \lambda_\eta^c, D_\eta) = u_\eta + \lambda_\eta^c - \frac{\sigma_\eta^t}{k_\eta},\tag{38}$$

$$\tilde{\lambda}_c(u_\eta, \lambda_\eta^t, D_\eta) = -u_\eta + \lambda_\eta^t - \frac{\sigma_\eta^c}{k_\eta}. \tag{39}$$

It is worth to note that the placement χ from (23) is a function only upon the position and time. Thus, the PDEs and BCs (31) have to be solved over the domain $\forall X \in \mathcal{B}$ and for every time $t = T_0, T_1, \ldots, T_M$. Besides, the irreversible kinematic descriptors in (24) are functions not only upon position X and time t but also upon the orientation \hat{c} . Thus, they have to be solved not only for every position of the domain, i.e. $\forall X \in \mathcal{B}$, and for every time, i.e. for every time $t = T_0, T_1, \ldots, T_M$, but also for every orientation, i.e. $\forall \hat{c} \in S^1$. Besides, the KKT conditions (32)–(33)–(34)–(35) are algebraic equations and therefore no Finite Element Method is necessary for their evaluation.

4. Characterization of the 2D granular micro-mechanics framework for the UHP FRC

4.1. Interpretation of the constitutive parameters of the granular micro-mechanic model

The model that we have recapped in the previous Section 3 depends upon only 9 parameters, i.e.

$$k_n^c, k_n^t, k_\tau, L, B, D_c^{mtr}, D_t^{mtr}, \sigma_n^t, \sigma_n^c$$

$$\tag{40}$$

The first three $(k_\eta^c, k_\eta^l \text{ and } k_\tau)$ are related to the elastic response from (5) with the inclusion of (6)–(13) and the fourth (L) to the characteristic size of the microstructure of the material. In Barchiesi et al. (2021) we have already proved that, in the case of tension–compression symmetry $(k_\eta = k_\eta^c = k_\eta^l)$ and for an isotropic elastic geometrically nonlinear material, the three parameters k_η, k_τ and L are related to the 2D Young's modulus Y_{2D} and Poisson's ratio v_{2D} ,

$$k_{\eta} = \frac{Y_{2D}}{\pi L^2 (1 - v_{2D})}, \qquad k_{\tau} = Y_{2D} \frac{1 - 3v_{2D}}{4\pi L^2 (1 - v_{2D}^2)}. \tag{41}$$

In this paper the deformation is, for the sake of simplicity, homogeneous and therefore strain gradient effects are not relevant. Moreover, the material is not at all an elastic one. However, the material is initially elastic and isotropic but with a different elastic behavior in tension and compression. In order to use the experimental results in (2)–(4), we assume a uniaxial homogeneous tension (or compression) deformation test along the orientation \hat{e}_1 , so that the Green Saint-Venant strain tensor G has the following null components,

$$G_{12} = G_{22} = 0. (42)$$

so that from (17), with the insertion of (15) and of (42), we have that the uniaxial stress S_{11} is

$$S_{11} = \mathbb{C}_{1111}G_{11} = \frac{\pi L^2}{4} \left(3k_{\eta} + 4k_{\tau} \right) G_{11}. \tag{43}$$

If we assume the validity of (41) in compression $(Y_{2D} = Y_{2D}^c)$

$$k_{\eta}^{c} = \frac{Y_{2D}^{c}}{\pi L^{2} (1 - v_{2D})}, \qquad k_{\tau} = Y_{2D} \frac{1 - 3v_{2D}}{4\pi L^{2} (1 - v_{2D}^{2})}, \tag{44}$$

the general form of the stress (43) with the inclusion of (i) the compression condition $k_\eta=k_\eta^c$, (ii) the identification (44) and (iii) the experimental law (1) with (2) yield,

$$S_{11} = \frac{\pi L^2}{4} \left(3k_{\eta}^c + 4k_{\tau} \right) G_{11} = \frac{Y_{2D}^c}{\left(1 - V_{2D}^2 \right)} G_{11} = S_{11}^{3D} A = E_c G_{11} A_c$$
 (45)

so that the identification of k_n^c and k_τ is derived from (44) and (45),

$$k_{\eta}^{c} = E_{c} \frac{1 + v_{2D}}{\pi L^{2}} A_{c}, \qquad k_{\tau} = E_{c} \frac{1 - 3v_{2D}}{4\pi L^{2}} A_{c}.$$
 (46)

It is worth to note that S_{11} is the component of the stress for the present 2D case and S_{11}^{3D} is the analogous component in a 3D case. If the thickness is assumed to be equal to A then their relation is $S_{11}=S_{11}^{3D}A$. Besides, in the compression test of Fig. 1, where we identify E_c in (2), the thickness is $A=A_c=10$ cm. In tension the general form of the stress (43) with the inclusion of (i) the tension condition $k_\eta=k_\eta^t$ and the experimental law (3) with (4) yield,

$$S_{11} = \frac{\pi L^2}{4} \left(3k_{\eta}^t + 4k_{\tau} \right) G_{11} = S_{11}^{3D} A = E_t G_{11} A_t \tag{47}$$

so that the identification of k_n^t is derived from (46) and (47)₂,

$$k_{\eta}^{t} = \frac{4}{3} \frac{E_{t} A_{t}}{\pi L^{2}} - \frac{4}{3} k_{\tau}. \tag{48}$$

It is worth to note that in the tension test of Fig. 3, where we identify E_t in (4), the thickness is extrapolated from Fig. 2, i.e. $A = A_t = 80$ mm.

From (37) B is interpreted as the characteristic tangent damage relative displacement. From (36) the interpretation of B as the characteristic normal damage relative displacement cannot be done as it was done in Maksimov et al. (2021), Placidi et al. (2022), Timofeev et al. (2021), Placidi et al. (2021) because of the presence of plastic multipliers in the KKT conditions that comes from a novel form of the dissipation energy functional in (18). However, for the sake of simplicity, we call B the characteristic damage displacement. From (36) and (37) it is evident that the higher the B, the lower is, for a given deformation process, the velocity of the damage evolution and for a given value of B one needs the same value for the relative displacements (e.g. tangential displacement $u_r \simeq B$) to achieve a non negligible value (i.e. $(1-D_{mtr}-e^{-1})/(1-D_{mtr})$) for tangential damage.

Let us calculate the 4 thresholds \tilde{D}_{η} , \tilde{D}_{τ} , $\tilde{\lambda}_{t}$ and $\tilde{\lambda}_{c}$ from (36)–(37)–(38)–(39) at the beginning of the deformation process, i.e for which the relative displacements u_{η} and u_{τ} and the damage D_{η} and D_{τ} and plastic λ_{η}^{t} and λ_{η}^{c} variables are all null,

$$\begin{split} \tilde{D}_{\eta}(0,0,0) &= \tilde{D}_{\tau}(0,0,0) = 1 - \frac{1}{1 - D_{mtr}} = -\frac{D_{mtr}}{1 - D_{mtr}}, \\ \tilde{\lambda}_{t}(0,0,0) &= -\frac{\sigma_{\eta}^{t}}{k_{\eta}}, \qquad \tilde{\lambda}_{c}(0,0,0) = -\frac{\sigma_{\eta}^{c}}{k_{\eta}}, \quad \forall \pmb{X} \in \mathcal{B}, \quad \forall \hat{c} \in \mathcal{S}^{1}. \end{split}$$

They are all negative once one adopts the following restrictions

$$k_{\eta} > 0$$
, $\sigma_{\eta}^{t} > 0$, $\sigma_{\eta}^{c} > 0$, $0 < D_{mtr} < 1$.

This is an important choice because, being all null the initial values of the 4 non-decreasing descriptors

$$D_{\eta} = D_{\tau} = \lambda_{\eta}^{t} = \lambda_{\eta}^{c} = 0, \quad at \quad t = 0$$
 (49)

the KKT conditions (32)–(33)–(34)–(35) are not solved with the curled parentheses, i.e. with

$$D_n = \tilde{D}_n, \quad D_{\tau} = \tilde{D}_{\tau}, \quad \lambda_n^t = \tilde{\lambda}_t, \quad \lambda_n^c = \tilde{\lambda}_c$$
 (50)

but with prescribing no increments, i.e. with

$$\Delta D_n = \Delta D_{\tau} = \Delta \lambda_n^t = \Delta \lambda_n^c = 0, \quad \forall X \in \mathcal{B}, \quad \forall \hat{c} \in \mathcal{S}^1$$

Besides, in order to solve the KKT conditions (32)–(33)–(34)–(35) with the curled parentheses and therefore to achieve a condition for damage and plastic evolution one needs to achieve an amount of relative displacements to make null the 4 thresholds \tilde{D}_{η} , \tilde{D}_{τ} , $\tilde{\lambda}_{t}$ and $\tilde{\lambda}_{c}$. In the following we will consider null, as in the initial condition (49), damage and plastic descriptors and make specific such amounts of relative displacements. From (36) the norm $\|u_{\eta}\|$ of the normal displacement needs to be equal to the positive number $\tilde{u}_{\eta D}$,

$$||u_{\eta}|| = \bar{u}_{\eta D} = -B \log (1 - D_{mtr}).$$
 (51)

From (37) the norm $\sqrt{\left(u_{\tau}\right)^2}$ of the tangent displacement needs to be equal to the positive number $\bar{u}_{\tau D}$

$$\sqrt{(u_{\tau})^2} = \bar{u}_{\tau D} = -B \log (1 - D_{mtr}).$$
 (52)

From (38) the normal displacement u_{η} needs to be positive and equal to the positive number $\bar{u}_{\eta\lambda l}$,

$$u_{\eta} = \bar{u}_{\eta \lambda t} = \frac{\sigma_{\eta}^{t}}{k_{u}}.\tag{53}$$

From (39) the normal displacement u_{η} needs to be negative and equal to the negative number $\bar{u}_{\eta \lambda c}$,

$$u_{\eta} = \bar{u}_{\eta\lambda c} = -\frac{\sigma_{\eta}^{c}}{k_{-}}.\tag{54}$$

Thus, the quantities D_{mir} (D_r^{mir} if the orientation is in tension and D_c^{mir} if the orientation is in compression according to (21)), σ_t^I and σ_r^C are related to those relative displacement values that are necessary to activate damage and plastic evolution according to (51)–(52)–(53)–(54).

4.2. Identification of the constitutive parameters of the granular micromechanic model

Let us first assume a characteristic size ${\cal L}$ of the microstructure to be

$$L = 10 \text{ mm}. \tag{55}$$

A better characterization of this size will be achieved in another publication dedicated to the non-homogeneous case, where the size of the strain localization will be of the same order of magnitude of the characteristic size L because of a different and strain gradient representation of the relative displacement (8)–(9).

By analyzing the first elastic stages in Figs. 1 and 3 we have achieved the values of elastic stiffness in tension and in compression in (2)–(4). By assuming a standard value

$$v_{2D} \cong 0.2, \tag{56}$$

for the 2D Poisson ratio, from (46)–(48) and the insertion in it of (2)–(4)–(55)–(56), we have the following numerical identifications,

$$k_n^c = 1.74 \times 10^{13} \text{ N/m}^3, k_n^t = 5.37 \times 10^{12} \text{ N/m}^3, k_\tau = 1.45 \times 10^{12} \text{ N/m}^3.$$
 (57)

Let us consider the uniaxial test defined in (42). Insertion of (42) into (8) yields the corresponding normal displacement as a function of the orientation \hat{c} ,

$$u_{\eta} = LG_{11}\hat{c}_{1}^{2},\tag{58}$$

where \hat{c}_1 is the first component of the unit vector \hat{c} . Thus, the orientation that suffers the maximum normal displacement u_{η}^{\max} is in this case $\hat{c}=\hat{e}_1$, i.e. the maximum normal displacement u_{η}^{\max} is achieved by insertion of $\hat{c}_1=1$ into (58),

$$u_n^{\max} = LG_{11}. (59)$$

Let $G_{11}^t>0$ be the value of the strain component G_{11} for which we activate damage and plastic evolution in tension and let $G_{11}^c>0$ be its opposite value in compression. In other words, we assume that damage and plastic evolution are activated for the same values in tension (at $G_{11}=G_{11}^t$) and in compression (at $G_{11}=-G_{11}^c$). Thus, we have from (21)–(51)–(52)–(53)–(54)–(59) the following relations,

$$LG_{11}^{t} = -B\log\left(1 - D_{t}^{mtr}\right) = \frac{\sigma_{\eta}^{t}}{k_{\eta}^{t}}, \quad LG_{11}^{c} = -B\log\left(1 - D_{c}^{mtr}\right) = -\frac{\sigma_{\eta}^{c}}{k_{\eta}^{c}},$$

which yield the identifications of the remaining constitutive coefficients as a functions of G_{11}^r and G_{11}^c ,

$$\sigma_{\eta}^{t} = k_{\eta}^{t} L G_{11}^{t}, \quad D_{t}^{mtr} = 1 - \exp\left(-\frac{L G_{11}^{t}}{B}\right),$$

$$\sigma_{\eta}^{c} = -k_{\eta}^{c} L G_{11}^{c}, \quad D_{c}^{mtr} = 1 - \exp\left(-\frac{L G_{11}^{c}}{B}\right).$$
(60)

By analyzing the ends of the elastic stages in Figs. 1 and 3 we guess the following values the strain-thresholds,

$$G_{11}^t = 0.0003, \qquad G_{11}^c = -0.0032.$$
 (61)

It is worth to note that it is also possible to use the CDP (Concrete Damage Plasticity) model (Simulia, 2014; Qingfu et al., 2020) to achieve similar values for the identifications (61). A parametric analysis can also be done for the characteristic damage displacement *B*. With the following hypothesis,

$$B = 1.5 \times 10^{-5} \text{ m},\tag{62}$$

we report the identifications of the remaining constitutive coefficients from (60)–(61)–(62)

$$\sigma_{\eta}^{t} = 1.61 \times 10^{7} \text{ N/m}^{2}, \ \sigma_{\eta}^{c} = 5.56 \times 10^{8} \text{ N/m}^{2}, \ D_{t}^{mtr} = 0.181, \ D_{c}^{mtr} = 0.882.$$
(63)

We note here that damage-mechanism that drive the mechanical response of UHP FRC are not investigated in a way that it is possible to distinguish normal and tangential ones. For this reason, we use a unique characteristic damage displacement B in (62).

5. Numerical simulations of the 2D problem

5.1. Definition of the problem for the tension/compression case

Let us solve the problem for a squared shape body \mathcal{B} with those boundary conditions defined in Fig. 4.

If the imposed displacement $\delta(t)$ is positive, then we are in the tension case. Besides, after an initially increasing function of time let us have a subsequent unloading stage as it is shown on the top-left-hand side of Fig. 5. In formulae we have

$$\delta(t) = \delta_1 \sin \frac{2\pi t}{T}, \qquad t \in [0, t_f], \tag{64}$$

where δ_1 is the maximum imposed displacement, T is the oscillation period and t_f the final time of the simulation. In tension and compression the final time is $t_f=3T/10$, that is greater than T/4 to show the mentioned unloading stage. Besides, in shear the final time is $t_f=T/2$ in order to show the complete unloading stage.

According to the geometry of Fig. 4, we assume that the body $\mathcal B$ is a square of size A

$$A = 100 \text{ mm}.$$
 (65)

The displacement field

$$u = X + \chi(X, t) \tag{66}$$

of the continuum body \mathcal{B} is induced by the particular boundary conditions prescribed in Fig. 4 for all the points X of the domain \mathcal{B} without any need of Finite Element simulations,

$$u_1 = \frac{\delta(t)}{A} X_1, \quad u_2 = 0, \qquad \forall \mathbf{X} \in \mathcal{B}. \tag{67}$$

Thus, the components of the Green–Saint-Venant strain tensor are derived by insertion of (67), (11) and (66) into (10),

$$G_{11} = \frac{\delta(t)}{A} + \frac{1}{2} \left(\frac{\delta(t)}{A}\right)^2, \quad G_{12} = G_{22} = 0,$$
 (68)

the first of which is represented on the top-right-hand side of Fig. 5. In this case, the qualitative evolution of displacement and strain is the

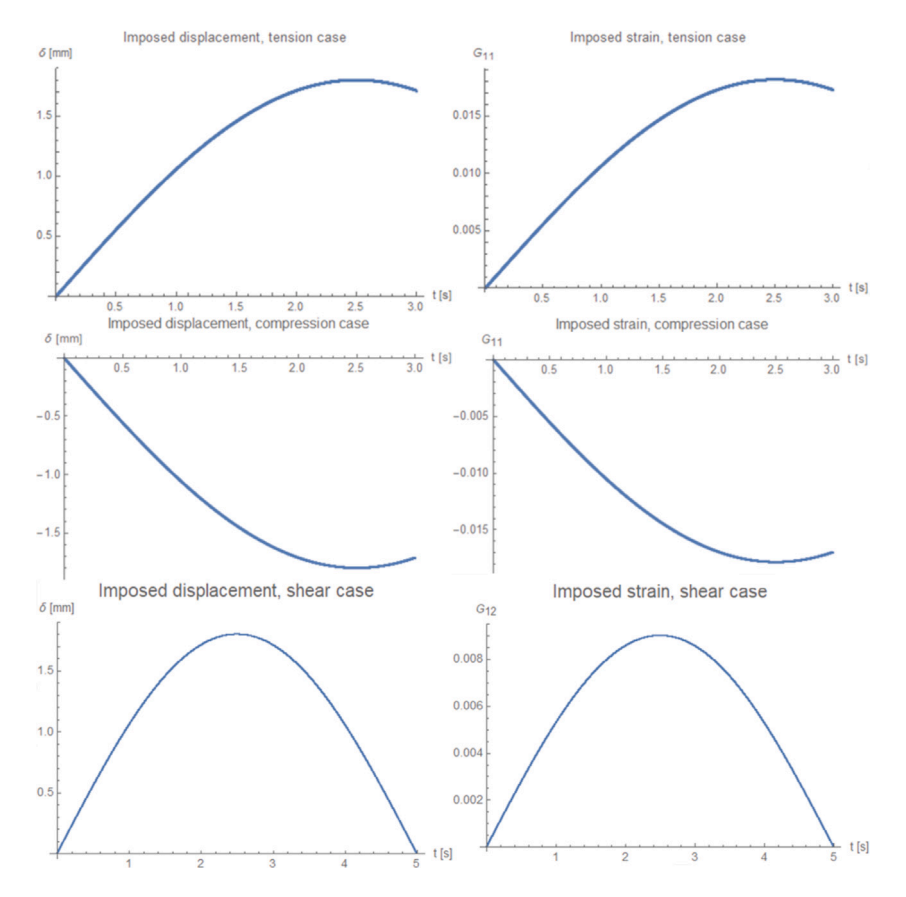


Fig. 5. Imposed displacement on the left-hand side and the components $G_{11}(t)$ or $G_{12}(t)$ of the imposed strain on the right-hand side, linked via the nonlinear relation (68). In the first row, we plot the tension case. In the second row, we plot the compression case. In the third row, we plot the shear case.

same because the nonlinear addend in $(68)_1$ is negligible. It is worth to note that elimination of those supports along the horizontal boundaries in Fig. 4 would imply non-homogeneous deformation and therefore the necessity of a Finite Element simulation for the calculation of the displacement field, that will be therefore different of (67).

It is worth mentioning that the displacement and strain fields in compression have the same representation of eqns. (67)–(68) but with opposite sign of the imposed displacement $\delta(t)$. They are represented in the second row of Fig. 5.

The normal and the squared tangent displacement from (8) and (9) yield,

$$u_{\eta} = LG_{11}\cos^{2}\theta = L\left[\frac{\delta(t)}{A} + \frac{1}{2}\left(\frac{\delta(t)}{A}\right)^{2}\right]\cos^{2}\theta,$$

$$u_{\tau}^{2} = 4L^{2}G_{11}G_{11}\left(\cos^{2}\theta - \cos^{4}\theta\right) = \left(L\left[\frac{\delta(t)}{A} + \frac{1}{2}\left(\frac{\delta(t)}{A}\right)^{2}\right]\sin 2\theta\right)^{2},$$
(70)

where a standard parameterization of the unit vector \hat{c} has been used in terms of an angle θ , i.e.,

$$\hat{c}_1 = \cos \theta, \quad \hat{c}_2 = \sin \theta. \tag{71}$$

The stress response is given in terms of the components S_{11} , S_{12} and S_{22} of the stress tensor in (17), with the use of (68)₂₃,

$$S_{11} = \mathbb{P}_{11} + \mathbb{C}_{1111}G_{11}, \quad S_{12} = \mathbb{P}_{12} + \mathbb{C}_{1211}G_{11}, \quad S_{22} = \mathbb{P}_{22} + \mathbb{C}_{2211}G_{11},$$

that, by insertion of (15) and (16), implies the following form of the stress tensor components.

$$S_{11} = -L \int_0^{2\pi} \left[k_\eta \left(1 - D_\eta \right) \left(\lambda_\eta^t - \lambda_\eta^c \right) \cos^2 \theta \right] d\theta + \tag{72}$$

$$+G_{11}L^{2}\int_{0}^{2\pi} \left[k_{\eta}\left(1-D_{\eta}\right)\cos^{4}\theta+k_{\tau}\left(1-D_{\tau}\right)\sin^{2}2\theta\right]d\theta,$$

$$S_{22} = -L\int_{0}^{2\pi} \left[k_{\eta}\left(1-D_{\eta}\right)\left(\lambda_{\eta}^{t}-\lambda_{\eta}^{c}\right)\sin^{2}\theta\right]d\theta+$$

$$+G_{11}L^{2}\int_{0}^{2\pi}\sin^{2}\theta\cos^{2}\theta\left[k_{\eta}\left(1-D_{\eta}\right)-4k_{\tau}\left(1-D_{\tau}\right)\right]d\theta,$$

$$S_{12} = -L\int_{0}^{2\pi} \left[k_{\eta}\left(1-D_{\eta}\right)\left(\lambda_{\eta}^{t}-\lambda_{\eta}^{c}\right)\sin\theta\cos\theta\right]d\theta+$$

$$+G_{11}L^{2}\int_{0}^{2\pi}\sin\theta\cos\theta\left[k_{\eta}\left(1-D_{\eta}\right)\cos^{2}\theta-k_{\tau}\left(1-D_{\tau}\right)\left[2\cos2\theta\right]\right]d\theta$$

$$(74)$$

Let us analyze the horizontal stress S_{11} . In the elastic phase (where all the damage and plastic descriptors are null) it is a linear function of the imposed strain G_{11} . The coefficient of such a linear dependence, i.e. the component \mathbb{C}_{1111} of the stiffness tensor, can be interpreted as an equivalent stiffness,

$$k_{eq}(t) = \mathbb{C}_{1111} = L^2 \int_0^{2\pi} \left[k_{\eta} \left(1 - D_{\eta} \right) \cos^4 \theta + k_{\tau} \left(1 - D_{\tau} \right) \sin^2 2\theta \right] d\theta$$
(75)

that evolves in time according to the evolution of damage descriptors D_{η} and D_{τ} . The equivalent stiffness in (75) provides a natural definition of an equivalent damage variable $d_{eg}(t)$, viz.,

$$k_{eq}(t) = k_{eq}^{0} \left[1 - d_{eq}(t) \right].$$
 (76)

where k_{eq}^0 is the initial value $k_{eq}\left(0\right)$ of the equivalent stiffness $k_{eq}\left(t\right)$,

$$k_{eq}(0) = k_{eq}^{0} = L^{2} \int_{0}^{2\pi} \left[k_{\eta} \cos^{4} \theta + k_{\tau} \sin^{2} 2\theta \right] d\theta = \frac{3\pi}{4} L^{2} k_{\eta} + \pi L^{2} k_{\tau}.$$
(77)

It is worth to note that in those tension and compression cases that are here defined, the orientations are all in tension or all in compression. This is the reason why k_η in (77) is k_η^t in tension and k_η^c in compression. Finally, the equivalent damage variable $d_{eq}(t)$ can be easily computed from (75)–(76)–(77),

$$d_{eq}(t) = 1 - \frac{k_{eq}(t)}{k_{eq}^0}. (78)$$

It is worth to note that the equivalent damage evolution in (78) does not give a complete description of the material behavior that can be deduced in this model. On the one hand, the load prescribed in Fig. 5 induces also (i) an evolution of the load free configuration from \mathbb{P}_{11} that can be calculated by the first addend of (72) and (ii) a lateral reaction, because of Poisson effect, that can be deduced by the component S_{22} in (73). On the other hand, the initial isotropic sample becomes anisotropic because damage and plastic variables evolves according to normal (69) and tangential (70) displacements that depend both upon the orientation θ . This implies, e.g., that the ratio

$$r(t) = \frac{\mathbb{C}_{1111}}{\mathbb{C}_{2222}} \tag{79}$$

between horizontal and vertical stiffness, initially equal to the unity value because of the assumed isotropy of the initial condition, becomes lower than 1. The reason is that the horizontal deformation is higher than the vertical one and therefore the corresponding stiffness is automatically reduced as a consequence of the deformation. The formal definitions of the equivalent damage (78), with the use of (75) and (77), and of the anisotropic index (79), with the use of (15), are the same in tension and in compression and will be computed in Sections 5.4.1 and 5.4.2.

Besides, the fourth order stiffness tensor \mathbb{C} can be reduced to a second order one, namely \mathfrak{C} , with the use of the Voigt notation for the representation of (17) in the following form,

$$\left(\begin{array}{c} S_{11} \\ S_{22} \\ S_{12} \end{array} \right) = \left(\begin{array}{c} S_{11} \\ S_{22} \\ S_{12} \end{array} \right) + \left(\begin{array}{ccc} \mathbb{C}_{1111} & \mathbb{C}_{1122} & 2\mathbb{C}_{1112} \\ \mathbb{C}_{1122} & \mathbb{C}_{2222} & 2\mathbb{C}_{1222} \\ 2\mathbb{C}_{1112} & 2\mathbb{C}_{1222} & 2\mathbb{C}_{1212} \end{array} \right) \left(\begin{array}{c} G_{11} \\ G_{22} \\ G_{12} \end{array} \right),$$

where the second order stiffness tensor $\mathfrak C$ is

$$\mathfrak{C} = \begin{pmatrix} \mathbb{C}_{1111} & \mathbb{C}_{1122} & 2\mathbb{C}_{1112} \\ \mathbb{C}_{1122} & \mathbb{C}_{2222} & 2\mathbb{C}_{1222} \\ 2\mathbb{C}_{1112} & 2\mathbb{C}_{1222} & 2\mathbb{C}_{1212} \end{pmatrix}. \tag{80}$$

The three eigenvalues of the second order stiffness tensor $\mathfrak C$ have an important interpretation. In fact, two of these eigenvalues are the same in the isotropic case and another measure for anisotropy is their split.

It is worth to finally note that the tension/compression asymmetry in the initial elastic stage induce a non-symmetric Poisson effect. To prove this fact, let us calculate the horizontal S_{11} and the vertical S_{22} stress components by insertion of the null damage condition (49) and the identifications (46)–(48) into (72)–(73) in compression,

$$S_{11} = G_{11}L^2 \frac{\pi}{4} \left(3k_\eta^c + 4k_\tau \right) = S_{11}^{3D} A_c = G_{11} E_c A_c, \tag{81}$$

$$S_{22} = G_{11}L^2 \frac{\pi}{4} \left(k_{\eta}^c - 4k_{\tau} \right) = S_{22}^{3D} A_c = G_{11} E_c v_{2D} A_c, \tag{82}$$

and in tension

$$S_{11} = G_{11}L^2 \frac{\pi}{4} \left(3k_{\eta}^t + 4k_{\tau} \right) = S_{11}^{3D} A_t = G_{11} E_t A_t, \tag{83}$$

$$S_{22} = G_{11}L^2 \frac{\pi}{4} \left(k_{\eta}^t - 4k_{\tau} \right) = S_{22}^{3D} A_t = G_{11} \left[v_{2D} E_c + \frac{1}{3} \left(E_t - E_c \right) \right] A_t. (84)$$

Thus, it is evident that the Poisson ratio v_{2D}^c in compression is from (81)–(82),

$$v_{2D}^c = \frac{S_{22}}{S_{11}} = v_{2D},$$

which is different from that v_{2D}^t in tension, that can be computed by (83)–(84).

$$v_{2D}^{t} = \frac{S_{22}}{S_{11}} = v_{2D} \frac{E_c}{E_t} + \frac{1}{3} \left(1 - \frac{E_c}{E_t} \right). \tag{85}$$

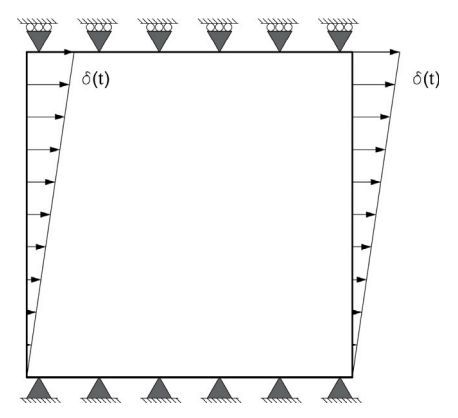


Fig. 6. Shear (Dirichlet-type) boundary conditions for a squared shape body \mathcal{B} induce homogeneous deformation reported in (87).

As a matter of facts the tension/compression symmetric condition $E_c=E_t$ implies from (85) an equivalent value $v_{2D}^c=v_{2D}^t$ of the Poisson ratio both in tension and in compression. However, in our case, $E_c/E_t \simeq 2$ and therefore from (56) and (85), we have $v_{2D}^t \simeq 0.07$.

5.2. Definition of the problem for the shear case

Let us solve the problem for the squared shape body \mathcal{B} with the same size (65) but with different boundary conditions defined in Fig. 6.

The displacement field u of the continuum body $\mathcal B$ is induced by the particular boundary conditions prescribed in Fig. 6 for all the points X of the domain $\mathcal B$ without any need of Finite Element simulations,

$$u_1 = \frac{\delta(t)}{A} X_2, \quad u_2 = 0, \qquad \forall \mathbf{X} \in \mathcal{B},$$
 (86)

where we assume the same function $\delta(t)$ of eqn. (64). The components of the Green–Saint-Venant strain tensor are derived by insertion of (86), (11) and (66) into (10),

$$G_{11} = 0, \quad G_{12} = \frac{\delta(t)}{2A}, \quad G_{22} = \frac{1}{2} \left(\frac{\delta(t)}{A}\right)^2,$$
 (87)

the second of which is represented on the bottom-right-hand side of Fig. 5. The third component is due to the geometrical nonlinearity of the formulation and is negligible for the present small deformation case.

The normal and the squared tangent displacement from (8)–(9) and (87) yield,

$$u_{\eta} = 2L \frac{\delta(t)}{2A} \left(\sin 2\theta + \frac{\delta(t)}{2A} \cos^2 \theta \right), \tag{88}$$

$$u_{\tau}^{2} = \left[L\left(\frac{\delta(t)}{2A}\right) \left(\cos 2\theta + \frac{\delta(t)}{2A}\sin 2\theta\right) \right]^{2},\tag{89}$$

where the parameterization (71) has been used for the orientation \hat{c} . It is worth to note that for small displacement and positive δ , we calculate from the sign of $\sin 2\theta$ in (88) the tension/compression discrimination in the present shear case,

$$\theta \in \left(0, \frac{\pi}{2}\right) \cup \left(\pi, \frac{3\pi}{2}\right), \quad \Rightarrow \quad k_{\eta} = k_{\eta}^{t},$$
 (90)

$$\theta \in \left(\frac{\pi}{2}, \pi\right) \cup \left(\frac{3\pi}{2}, 2\pi\right), \quad \Rightarrow \quad k_{\eta} = k_{\eta}^{c}.$$
 (91)

The stress response is given in terms of the components S_{11} , S_{22} and S_{12} of the stress tensor in (17), with the use of (87)₁,

$$S_{11} = \mathbb{P}_{11} + 2\mathbb{C}_{1112}G_{12} + \mathbb{C}_{1122}G_{22},$$

$$S_{22} = \mathbb{P}_{22} + 2\mathbb{C}_{2212}G_{12} + \mathbb{C}_{2222}G_{22},$$

$$S_{12} = \mathbb{P}_{12} + 2\mathbb{C}_{1212}G_{12} + \mathbb{C}_{1222}G_{22},$$

that, by insertion of (15) and (16), implies the following form of the stress tensor components,

$$S_{11} = -L \int_{0}^{2\pi} k_{\eta} \left(1 - D_{\eta} \right) \left(\lambda_{\eta}^{t} - \lambda_{\eta}^{c} \right) \cos^{2}\theta d\theta +$$

$$+2G_{12}L^{2} \int_{0}^{2\pi} \cos\theta \sin\theta \left[k_{\eta} \left(1 - D_{\eta} \right) \cos^{2}\theta - k_{\tau} \left(1 - D_{\tau} \right) 2 \cos 2\theta \right] d\theta +$$

$$+G_{22}L^{2} \int_{0}^{2\pi} \sin^{2}\theta \cos^{2}\theta \left[k_{\eta} \left(1 - D_{\eta} \right) - 4k_{\tau} \left(1 - D_{\tau} \right) \right] d\theta ,$$

$$S_{22} = -L \int_{0}^{2\pi} k_{\eta} \left(1 - D_{\eta} \right) \left(\lambda_{\eta}^{t} - \lambda_{\eta}^{c} \right) \sin^{2}\theta d\theta +$$

$$+2G_{12}L^{2} \int_{0}^{2\pi} \sin\theta \cos\theta \left[k_{\eta} \left(1 - D_{\eta} \right) \sin^{2}\theta + k_{\tau} \left(1 - D_{\tau} \right) 2 \cos 2\theta \right] d\theta +$$

$$+G_{22}L^{2} \int_{0}^{2\pi} \left[k_{\eta} \left(1 - D_{\eta} \right) \sin^{4}\theta + k_{\tau} \left(1 - D_{\tau} \right) \sin^{2}2\theta \right] d\theta ,$$

$$S_{12} = -L \int_{0}^{2\pi} k_{\eta} \left(1 - D_{\eta} \right) \left(\lambda_{\eta}^{t} - \lambda_{\eta}^{c} \right) \sin\theta \cos\theta d\theta +$$

$$+2G_{12}L^{2} \int_{0}^{2\pi} \left[k_{\eta} \left(1 - D_{\eta} \right) \sin^{2}\theta \cos^{2}\theta + k_{\tau} \left(1 - D_{\tau} \right) \cos^{2}2\theta \right] d\theta +$$

$$+2G_{12}L^{2} \int_{0}^{2\pi} \left[k_{\eta} \left(1 - D_{\eta} \right) \sin^{2}\theta \cos^{2}\theta + k_{\tau} \left(1 - D_{\tau} \right) \cos^{2}2\theta \right] d\theta +$$

$$+G_{22}L^{2} \int_{0}^{2\pi} \sin\theta \cos\theta \left[k_{\eta} \left(1 - D_{\eta} \right) \sin^{2}\theta + k_{\tau} \left(1 - D_{\tau} \right) \left[2 \cos 2\theta \right] \right] d\theta .$$

In order to propose an equivalent stiffness $k_{eq}^s(t)$ also for the shear case we analyze in the elastic phase (where all the damage and plastic descriptors are null) the shear stress S_{12} . It is a linear function of the shear strain G_{12} . The coefficient of such linear dependence, i.e. twice the component \mathbb{C}_{1212} of the stiffness tensor, can be interpreted as an equivalent shear stiffness,

$$k_{eq}^{s}(t) = 2C_{1212} = 2L^{2} \int_{0}^{2\pi} \left[k_{\eta} \left(1 - D_{\eta} \right) \sin^{2}\theta \cos^{2}\theta + k_{\tau} \left(1 - D_{\tau} \right) \cos^{2}2\theta \right] d\theta$$
(95)

that evolves in time according to the evolution of damage descriptors D_{η} and D_{τ} . The equivalent shear stiffness in (95) provides a natural definition of an equivalent shear damage variable $d_{eq}^{s}(t)$, viz.,

$$k_{eq}^{s}(t) = k_{eq}^{s0} \left[1 - d_{eq}^{s}(t) \right],$$
 (96)

where k_{eq}^{0s} is the initial value $k_{eq}^{s}(0)$ of the equivalent shear stiffness $k_{eq}^{s}(t)$. Such an initial stiffness,

$$k_{eq}(0) = k_{eq}^{s0} = 2L^2 \int_0^{2\pi} \left[k_{\eta} \sin^2 \theta \cos^2 \theta + k_{\tau} \cos^2 2\theta \right] d\theta,$$
 (97)

because of tension/compression asymmetry and the use of (90)-(91) is

$$k_{eq}^{s0} = \frac{\pi}{4}L^2 \left(k_{\eta}^c + k_{\eta}^t + 8k_{\tau} \right).$$

The equivalent shear damage variable $d_{eq}^{s}(t)$ can be easily computed from (96).

$$d_{eq}^{s}(t) = 1 - \frac{k_{eq}^{s}(t)}{k_{eq}^{s0}},$$
(98)

where (95) is used for the graphic of Fig. 15.

Even in this shear case, it is worth to note that the equivalent damage evolution in (98) does not give a complete description of the material behavior that can be deduced in this model. On the one hand, the load prescribed in Fig. 5 induces also (i) an evolution of the load free configuration from \mathbb{P}_{12} that can be calculated by the first addend of (94) and (ii) normal reactions can be deduced by the components S_{11} and S_{22} in (92)–(93). On the other hand, the initial isotropic sample becomes anisotropic because damage and plastic variables evolve according to normal (88) and tangential (89) displacements that depend both upon the orientation θ . This implies, e.g., that the ratio

$$r^{s}(t) = \frac{\mathbb{C}_{ijhk} n_{i}^{1} n_{j}^{1} n_{h}^{1} n_{k}^{1}}{\mathbb{C}_{ijhk} n_{i}^{2} n_{i}^{2} n_{h}^{2} n_{k}^{2}}$$
(99)

between two oblique stiffnesses, one along the oblique direction $n_i^1 = \delta_{i1} + \delta_{i2}$ and the other along the oblique direction $n_i^2 = -\delta_{i1} + \delta_{i2}$, initially equal to the unity value because of the assumed isotropy of the initial condition, becomes different than 1.

It is worth to note finally a qualitative difference between tension/compression cases and the shear case. In order to explain this concept in an easy way we consider the small displacement approximation. On the one hand, in the tension/compression cases and for a given value of the strain component G_{11} , normal and tangential displacement reach from (69) and (70) the same maximum values

$$u_n^{\max} = u_{\tau}^{\max} = LG_{11}.$$

On the other hand, in the shear case and for a given value of the strain component G_{12} , normal and tangential displacement reach from (88) and (89) different maximum values

$$u_{\eta}^{\text{max}} = 2u_{\tau}^{\text{max}} = 2LG_{12}.$$

In other words in the shear case, as it is expected, the maximum tangential displacement is larger than the maximum normal displacement. This implies that we have different regimes after the elastic one. The reason is that not only the thresholds in tension and in compression are reached at different level of the shear component G_{12} because of the different values prescribed in (63) but also the normal and tangential damage thresholds, see e.g. (51)–(52), are now reached at different values of the shear component G_{12} .

5.3. Numerical method for the homogeneous simulations

Some assumptions have been made in the initial stage of the process. The first is the initial null conditions not only for the displacement field *u*.

$$u(X, t = T_0) = 0, \quad \forall X \in \mathcal{B}$$

but also for damage and plastic descriptors:

$$\begin{split} D_{\eta}(\hat{c},\boldsymbol{X},t=T_{0}) &= 0, \qquad D_{\tau}(\hat{c},\boldsymbol{X},t=T_{0}) = 0, \qquad \forall \boldsymbol{X} \in \mathcal{B}, \forall \hat{c} \in \mathcal{S}^{1} \text{ (100)} \\ \lambda_{\eta}^{t}(\hat{c},\boldsymbol{X},t=T_{0}) &= 0, \qquad \lambda_{\eta}^{c}(\hat{c},\boldsymbol{X},t=T_{0}) = 0, \qquad \forall \boldsymbol{X} \in \mathcal{B}, \forall \hat{c} \in \mathcal{S}^{1} \text{ (101)} \end{split}$$

Isotropic initial condition is therefore deduced according to the eqns. (15)–(16). The algorithm of the simulation is very simple and deserves to be mentioned

We firstly consider the imposed displacement δ at the initial time step $t=T_1$ and deduce for that time, the displacement field u from (67) or (86). In the general non-homogeneous case such a deduction is not an easy task and a Finite Element approximation is needed. However, the purpose of this paper is to show the validity of a certain class of constitutive relations and to do this we have avoided to consider boundary conditions inducing non-homogeneous deformation. We have therefore selected a particular kind of boundary conditions for which homogeneous deformation is the solution and therefore there is no need of Finite Element modeling. Thus, the strain field G is calculated from (68) or (87) for every positions $\forall X \in \mathcal{B}$ and it is also calculated the normal and tangential displacement from (69)–(70) or (88)–(89) for every positions $\forall X \in \mathcal{B}$ and orientations $\forall \hat{c} \in \mathcal{S}^1$. Thus, we calculate the KKT conditions (32)–(33)–(34)–(35) and calculate for the time step $t=T_1$ damage and plastic descriptors:

$$\begin{split} D_{\eta}(\hat{c},\boldsymbol{X},t=T_1), & D_{\tau}(\hat{c},\boldsymbol{X},t=T_1), & \forall \boldsymbol{X} \in \mathcal{B}, \forall \hat{c} \in \mathcal{S}^1, \\ \lambda_{\eta}^{l}(\hat{c},\boldsymbol{X},t=T_1), & \lambda_{r}^{s}(\hat{c},\boldsymbol{X},t=T_1), & \forall \boldsymbol{X} \in \mathcal{B}, \forall \hat{c} \in \mathcal{S}^1. \end{split}$$

Thus, isotropic condition is not satisfied anymore and therefore the anisotropic stiffness tensors can be calculated analytically from (15)–(16) to deduce the stress components from (72)–(73)–(74) at time $t=\frac{T}{2}$

We secondly consider the imposed displacement δ at the second time step $t=T_2$ and repeat the procedure for all the time steps.

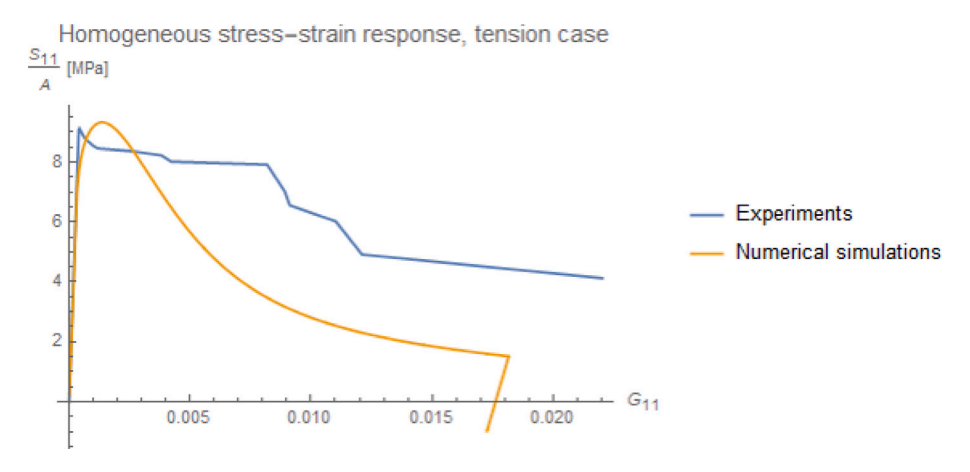


Fig. 7. Stress-strain response for the tension case. Numerical and experimental results are shown together.

5.4. Results of the homogeneous simulation

In this Subsection we show the numerical results for the homogeneous cases presented in Sections 5.1 and 5.2 and with the numerical method explicited in Section 5.3.

5.4.1. Tension case

The tension case is characterized with the positive value of the imposed displacement (64)

$$\delta_1 = 1.8 \text{ mm}.$$

In Fig. 7 we show the stress–strain response for the tension case. We have qualitative agreement with the experimental results reported in Fig. 3.

After the first elastic stage, at $G_{11} = G_{11}^t$ damage and plastic variables are activated by both the KKT (32)-(33)-(34)-(35) and initial (100)–(101) conditions. Because of the homogeneity of the strain, their evolution are independent upon position. However, because of the uniaxial loading, they are a function of the orientation. We report such a dependence in Fig. 8. We observe that normal damage and plastic tension accumulation displacement are higher for those orientations \hat{c} that are close to the uniaxial loading direction \hat{e}_1 , where the normal displacement is higher, i.e. with θ close to $k\pi$ with k being an integer number $k = 0, 1, 2, \dots$ Besides, the tangential damage is higher where the tangential displacement is higher, i.e. with θ close to $\frac{\pi}{4} + k \frac{\pi}{2}$ with k being an integer number k = 0, 1, 2, ... In this tension case all the orientations are in tension. Thus plastic accumulation in compression is null for every orientation and is not reported. The evolution of damage and plastic descriptors are shown in Fig. 8 at different levels of the applied strain. The first is, according to (61)₁ at the strain threshold of the elastic phase. The second is at 10 times such a threshold. The third is an intermediate one. The fourth is at the maximum value of the applied strain and the last is at the end of the time history. We observe that between the fourth and the fifth strain level we are in an unloading phase and therefore the damage and plastic descriptors do not evolve. Evolution of damage variables induces a non trivial evolution of both the equivalent damage d_{eq} from (78) and of the anisotropic index rfrom (79). Besides, two of the eigenvalues of the second order stiffness tensor defined in (80) are initially the same and the induced anisotropy is shown by the splitting of such two eigenvalues. The corresponding calculated functions are reported in Figs. 9. In particular, in Fig. 9a we show the equivalent damage d_{eq} and the anisotropic index r defined in (98) and (99), respectively, and in Fig. 9b we show the splitting of the two eigenvalues of the second order stiffness tensor for the tension case.

5.4.2. Compression case

The compression case is characterized with the negative value of the imposed displacement (64)

 $\delta_1 = -1.8 \text{ mm}.$

In Fig. 10 we show the stress–strain response for the compression case. We have qualitative agreement with the experimental results reported in Fig. 1.

After the first elastic stage, at $G_{11} = -G_{11}^c$ damage and plastic variables are activated by both the KKT (32)-(33)-(34)-(35) and initial (100)–(101) conditions. Because of the homogeneity of the strain, their evolution are independent upon position. However, because of the uniaxial loading, they are a function of the orientation. We report such a dependence in Fig. 11. We observe that normal damage and plastic tension accumulation displacement are higher for those orientations \hat{c} that are close to the uniaxial loading direction \hat{e}_1 , where the normal displacement is higher, i.e. with θ close to $k\pi$ with k being an integer number $k = 0, 1, 2, \dots$ Besides, the tangential damage is higher where the tangential displacement is higher, i.e. with θ close to $\frac{\pi}{4} + k \frac{\pi}{2}$ with k being an integer number $k = 0, 1, 2, \dots$ In this compression case all the orientations are in compression. Thus plastic accumulation in tension is null for every orientation and is not reported. The evolution of damage and plastic descriptors are shown in Fig. 11 at different levels of the applied strain. The first is, according to (61)2 at the strain threshold of the elastic phase. The second is at 2 times such a threshold. The third is an intermediate one. The fourth is at the maximum value of the applied strain and the last is at the end of the time history. We observe that between the fourth and the fifth strain level we are in an unloading phase and therefore the damage and plastic descriptors do not evolve. Evolution of damage variables induces a non trivial evolution of both the equivalent damage d_{eq} from (78) and of the anisotropic index rfrom (79). Besides, two of the eigenvalues of the second order stiffness tensor defined in (80) are initially the same and the induced anisotropy is shown by the splitting of such two eigenvalues. The corresponding calculated functions are reported in Fig. 12. In particular, in Fig. 12a we show the equivalent damage d_{eq} and the anisotropic index r defined in (98) and (99), respectively, and in Fig. 12b we show the splitting of the two eigenvalues of the second order stiffness tensor for the compression case.

5.4.3. Shear case

The shear case is characterized with the positive value, from (64), of the parameter δ_1 ,

 $\delta_1 = 1.8 \text{ mm}.$

In Fig. 13 we show the stress-strain response for the shear case. Here, we do not have experimental results for comparison. Thus, we show the

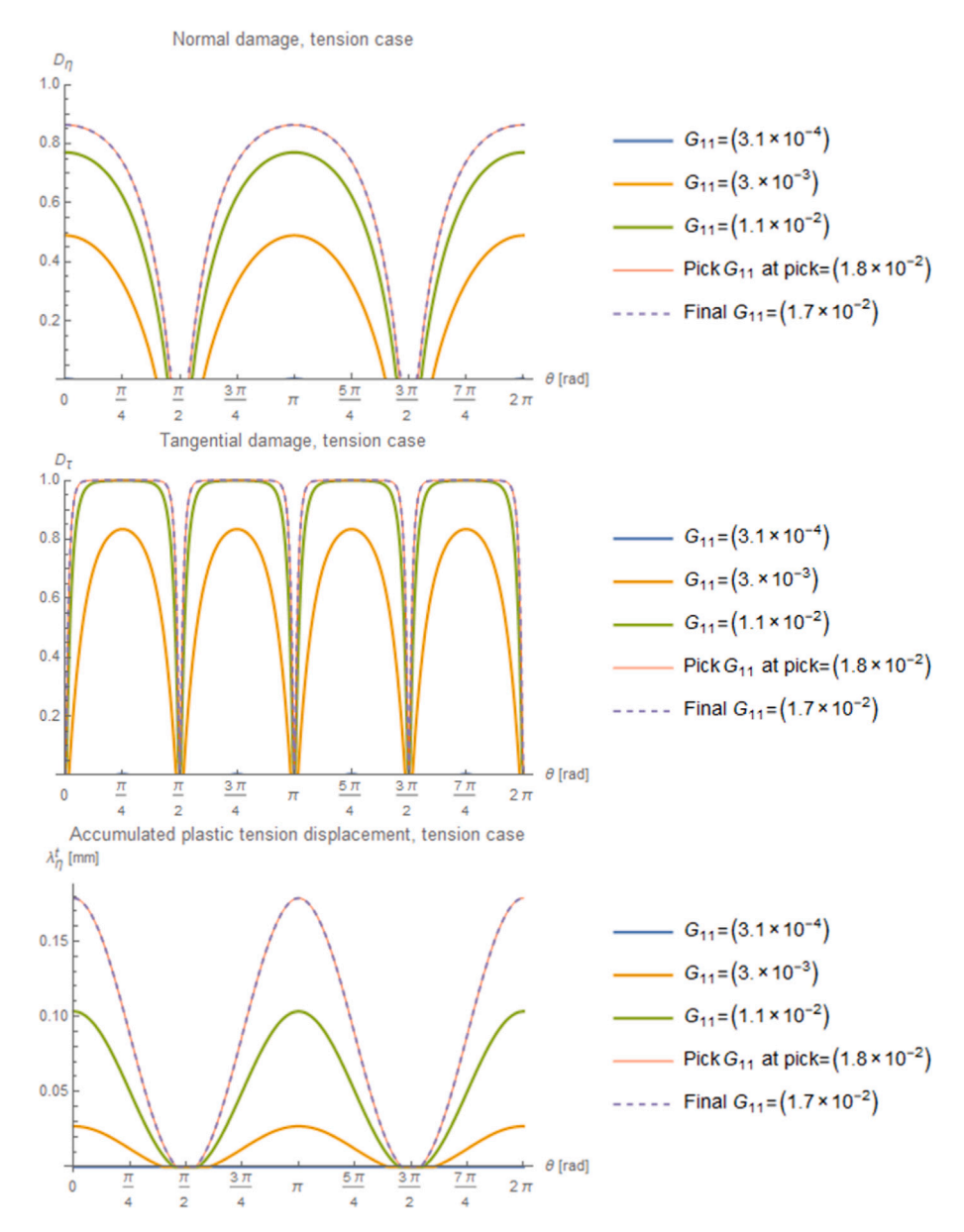


Fig. 8. Damage and plastic variables evolution in the tension case. All the orientations are in tension and therefore plastic accumulation in compression is null.

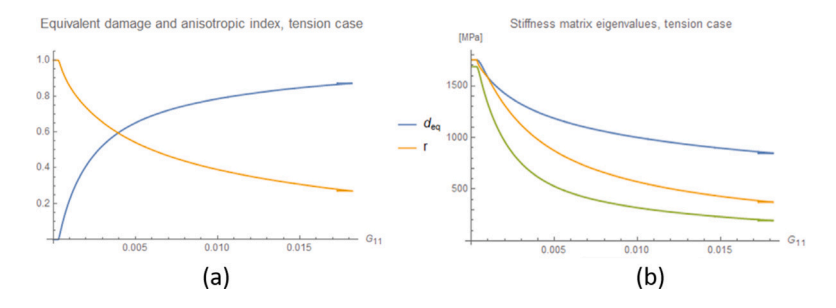


Fig. 9. (a) Equivalent damage and anisotropic index, defined in (98) and (99), in the tension case are plotted both as a function of the imposed strain. (b) Three eigenvalues of the second order stiffness tensor defined in (80).

results for the purpose to show the phenomenology of the presented constitutive prescriptions.

After the first elastic stage, damage and plastic variables are activated by both the KKT (32)–(33)–(34)–(35) and initial (100)–(101)

conditions. The activation of damage and plastic descriptors occur before for those orientations that are in tension, then tangential damage is activated and then for those orientations that are in compression according to the comments at the end of Section 5.2. Because of the

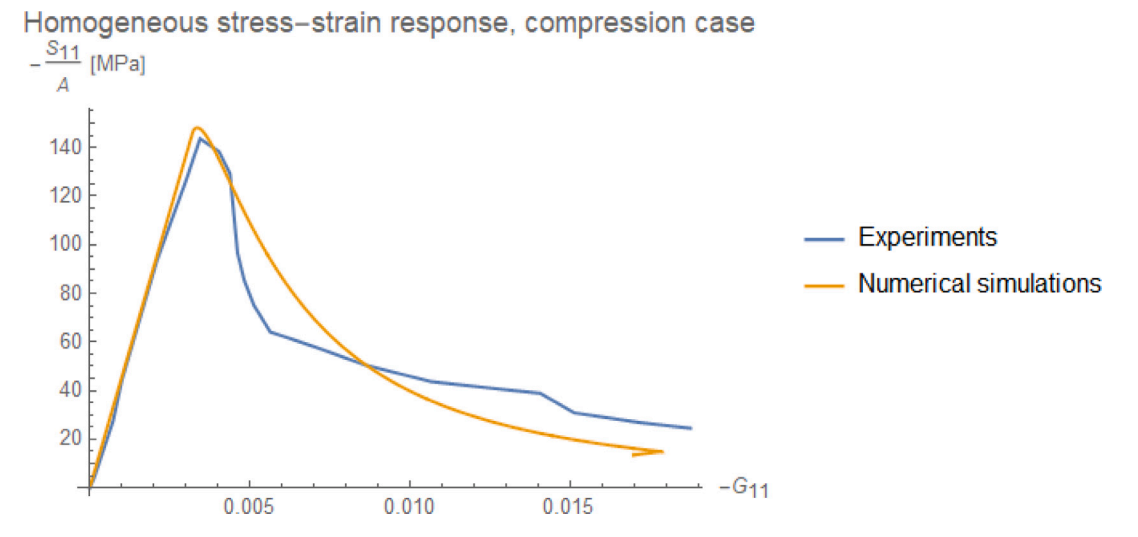


Fig. 10. Stress-strain response for the compression case. Numerical and experimental results are shown together.

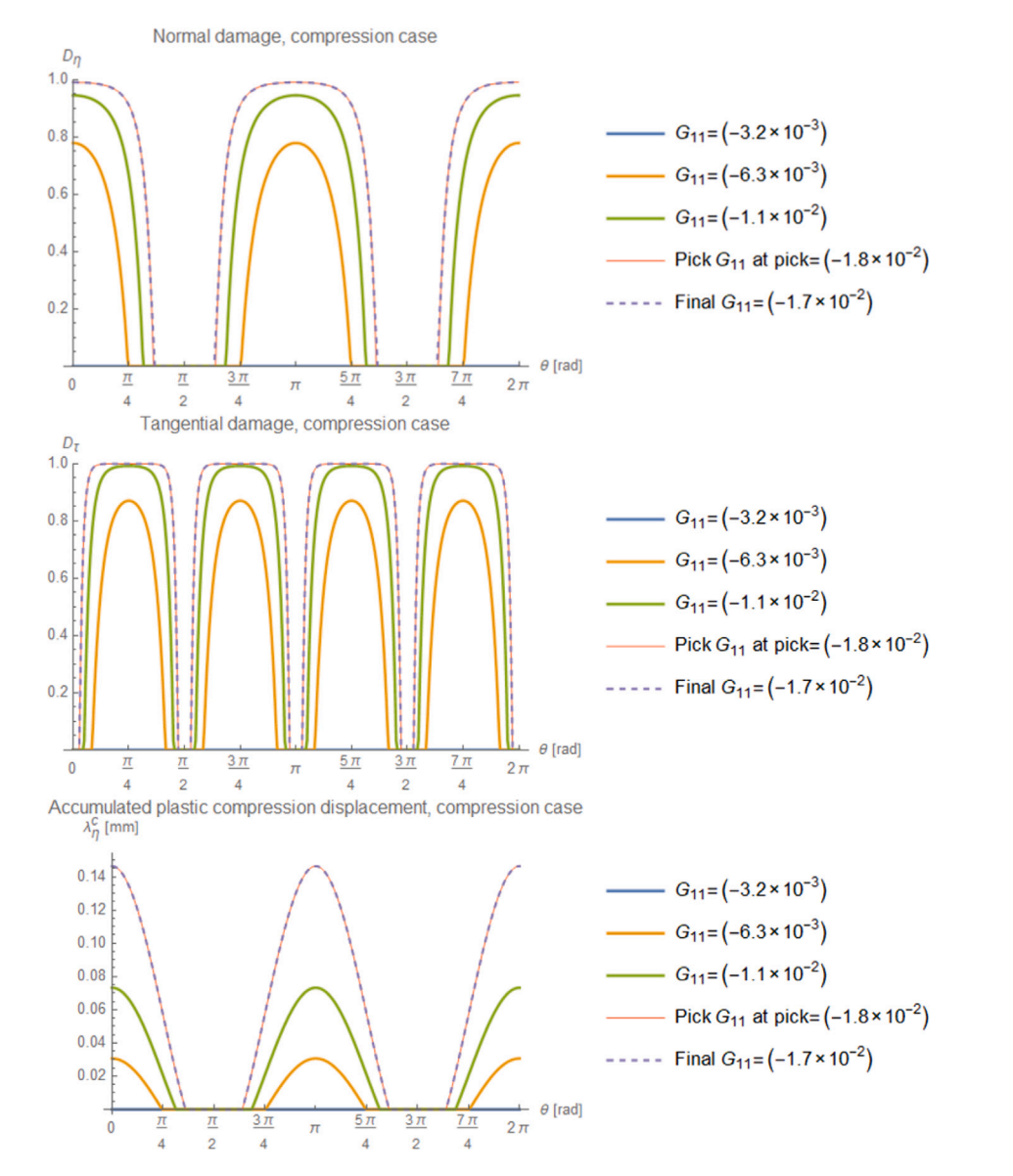


Fig. 11. Damage and plastic variables evolution in the compression case. All the orientations are in compression and therefore plastic accumulation in tension is null.

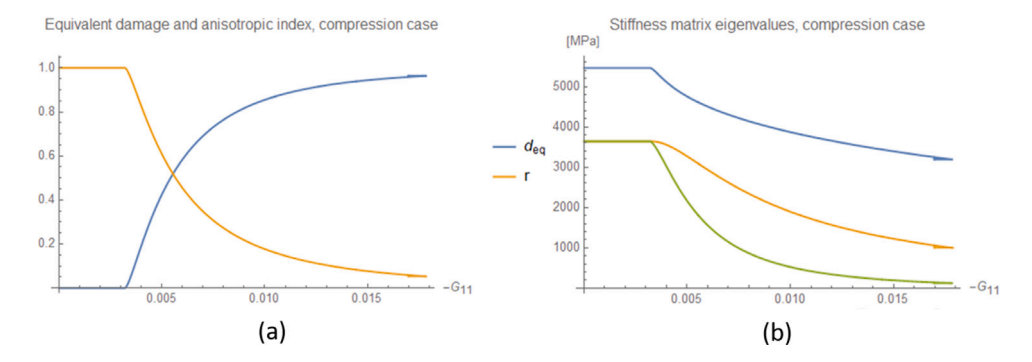


Fig. 12. (a) Equivalent damage and anisotropic index are plotted as a function of the imposed displacement for the compression case. (b) Three eigenvalues of the second order stiffness tensor defined in (80).

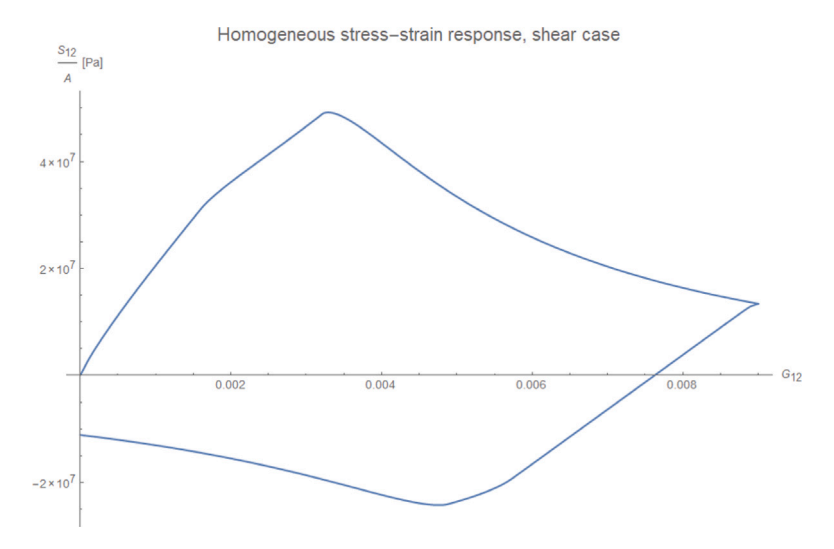


Fig. 13. Stress-strain response for the shear case.

homogeneity of the strain, the stress strain evolution of Fig. 13 is independent upon position. However, because of the shear loading, orientations evolve in a different way. We report such a dependence in Fig. 14. We observe that normal damage and plastic tension accumulation displacement are higher for those orientations \hat{c} that are close to the oblique direction $\hat{e}_1 + \hat{e}_2$, where the normal displacement is positive and higher. Thus, normal damage and plastic compression accumulation displacement are higher for those orientations \hat{c} that are close to the oblique direction $\hat{e}_1 - \hat{e}_2$, where the normal displacement is negative and higher in modulus. Besides, the tangential damage is higher where the tangential displacement is higher, i.e. with θ close to $k = 0, 1, 2, \dots$ In this shear case the orientations are some in tension and some in compression. Thus, both plastic accumulation in compression and in tension are not null for some orientations and they are therefore both reported. Evolution of damage variables induces a non trivial evolution of both the equivalent shear damage d_{eq}^s from (98) and of the anisotropic index r^s from (99). It is worth to note that, because of the tension-compression asymmetry, the sheared sample is anisotropic from the very beginning. This is shown by the fact that none of the eigenvalues of the second order stiffness tensor defined in (80) are initially the same. The corresponding calculated functions are reported in Figs. 15. In particular, in Fig. 12a we show the equivalent damage d_{eq}^{s} and the anisotropic index r^{s} and in Fig. 12b we show the three eigenvalues of the second order stiffness tensor for the shear case. It is worth to note that the equivalent damage is a monotonic variable both in the loading and in the unloading stages. However, in the abrupt switch between these two stages the tensioncompression asymmetry makes the equivalent damage to decrease

because the orientations in tension and that in compression change, at that point, the role and the equivalent stiffness increases.

6. Conclusion and outlook

The main thrust of the work is the adaptation of the granular micromechanics approach (GMA) developed in Barchiesi et al. (2021), Misra and Poorsolhjouy (2015), Misra and Singh (2015), Placidi et al. (2021), Timofeev et al. (2021), to the modeling of Ultra High Performance Fiber Reinforced Concrete (UHP FRC). We have shown that by properly defining the effective grain-pair damage-elasto-plastic spring elements in the normal and tangential directions, the response of UHP FRC under macro-scale homogeneous deformation can be modeled. The novel aspects of the introduced parameterized effective grain-pair damage-elasto-plastic spring elements include tension-compression asymmetric normal stiffnesses and characteristic damage relative displacement and the control for relative displacement necessary to activate damage and plastic evolution. A detailed methodology for determination of effective grain-pair model parameters from macro-scale measurements and their physical interpretation are discussed. The model is then applied to predict UHP FRC response under macroscale homogeneous deformation when subjected to uniaxial extension and compression as well as pure shear deformation. The prediction shows the model capability for describing gradual post peak softening that UHP FRC typically exhibits in both homogeneous extension and compression. More importantly, the model predicts that under such macro-scale homogeneous deformation, the evolution of damage and plasticity are directional, indicating an evolution of micro-scale mechanical and structural attributes that results in macro-scale anisotropy.

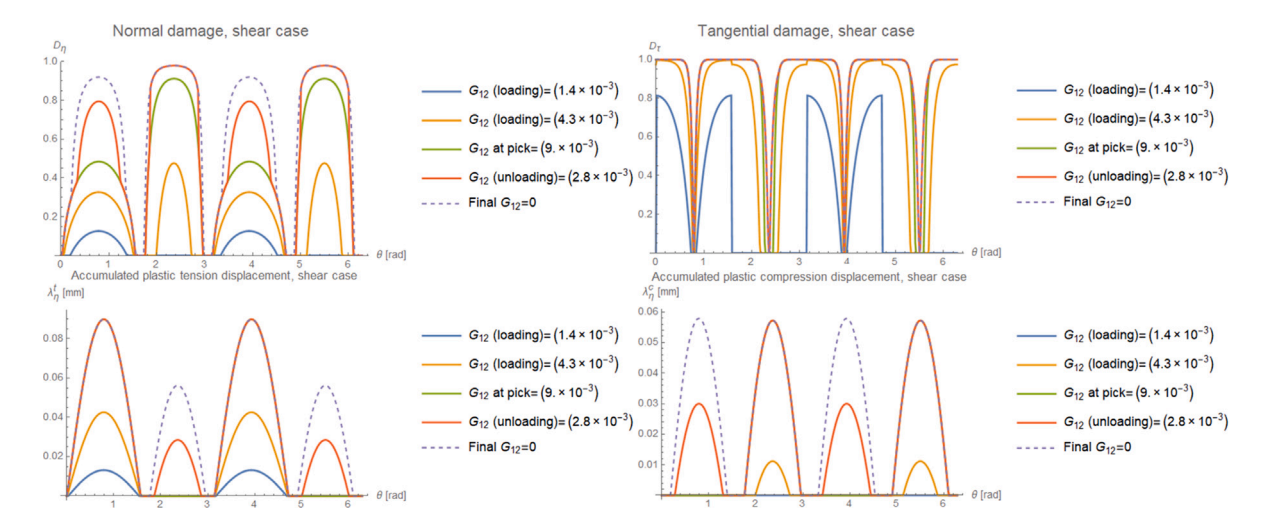


Fig. 14. Damage and plastic variables evolution in the shear case.

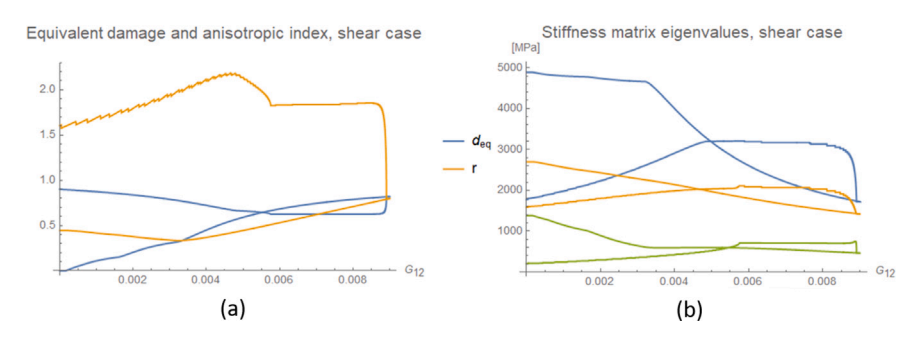


Fig. 15. (a) Equivalent shear damage and anisotropic index are plotted as a function of the imposed shear strain. (b) Three eigenvalues of the second order stiffness tensor defined in (80).

The directional nature of evolution that GMA based model is able to elaborate is particularly interesting for the case of pure shear in which certain grain-pair orientations experience tension while others undergo compression resulting in a non-monotonic evolution of macroscopic anisotropy. Finally, it is noteworthy that the derived model can be used to predict unloading to the stress free state (with non trivial plastic deformation) or to the strain free state (with the non trivial prestress prescribed in (16)). Future work will consider implementation of the approach to simulate cases with non-homogeneous deformations, such as the three-points bending test, in which the loading path at various material points can be unique and complex including certain materials suffering unloading while others experience loading. For such problem, second gradient theories are needed to not only regularize the numerical computations but to correctly describe the formation of strain localization zones and eventual fracture as in Placidi et al. (2021), Timofeev et al. (2021).

CRediT authorship contribution statement

Luca Placidi: Writing – review & editing, Writing – original draft, Visualization, Validation, Supervision, Software, Methodology, Investigation, Formal analysis, Data curation, Conceptualization. Francesco dell'Isola: Validation, Supervision, Methodology, Conceptualization. Abdou Kandalaft: Writing – review & editing, Writing – original draft, Visualization, Methodology, Investigation, Formal analysis, Data curation, Conceptualization. Raimondo Luciano: Writing – review & editing, Supervision, Methodology. Carmelo Majorana: Writing – review & editing, Writing – original draft, Supervision, Methodology, Investigation, Formal analysis, Conceptualization.

Declaration of competing interest

The authors declare that they have no known competing financial interests or personal relationships that could have appeared to influence the work reported in this paper.

Data availability

Data will be made available on request.

Acknowledgments

Research studies presented in this paper were supported partially by Innovative Bridge Technologies/Accelerated Bridge Construction University Transportation Center (IBT/ABC-UTC)ABC-UTC, funded by U.S. DOT under the University Transportation program. Opinions expressed in this paper are not necessarily those of the US DOT.

References

Abali, B.E., Müller, W.H., dell'Isola, F., 2017. Theory and computation of higher gradient elasticity theories based on action principles. Arch. Appl. Mech. 1–16.
 Abdou, Kandalaft, Vincenzo, Romanazzi, Francesco, Micelli, Maria, Aiello, 2022. Very

Abdou, Kandalaft, Vincenzo, Romanazzi, Francesco, Micelli, Maria, Aiello, 2022. Very high-performance fiber reinforced concrete (VHPFRC) testing and finite element analysis. RACTSI 2–5.

Aifantis, Elias C., 1984. On the microstructural origin of certain inelastic models. J. Eng. Mater. Technol. 106, 326–330.

Aifantis, Elias C., 1987. The physics of plastic deformation. Int. J. Plast. 3 (3), 211–247. Aifantis, Elias C., 1992. On the role of gradients in the localization of deformation and fracture. Internat. J. Engrg. Sci. 30 (10), 1279–1299.

Altenbach, H., Eremeyev, V., 2008. Analysis of the viscoelastic behavior of plates made of functionally graded materials. ZAMM J. Appl. Math. Mech./Z. Angew. Math. Mech. 88 (5), 332–341.

- Ambati, M., Gerasimov, T., Lorenzis, L., 2015. A review on phase-field models of brittle fracture and a new fast hybrid formulation.. Comput. Mech. 55 (2).
- Auffray, N., dell'Isola, F., Eremeyev, V., Madeo, A., Rosi, G., 2015a. Analytical continuum mechanics à la Hamilton-Piola least action principle for second gradient continua and capillary fluids. Math. Mech. Solids 20 (4), 375-417.
- Auffray, N., Dirrenberger, J., Rosi, G., 2015b. A complete description of bi-dimensional anisotropic strain-gradient elasticity. Int. J. Solids Struct. 69, 195–206.
- Barchiesi, Emilio, Misra, Anil, Placidi, Luca, Turco, Emilio, 2021. Granular micromechanics-based identification of isotropic strain gradient parameters for elastic geometrically nonlinear deformations. ZAMM J. Appl. Math. Mech./Z. Angew. Math. Mech. e202100059.
- Battista, A., Rosa, L., dell'Erba, R., Greco, L., 2016. Numerical investigation of a particle system compared with first and second gradient continua: Deformation and fracture phenomena. Math. Mech. Solids 1081286516657889.
- Bourdin, B., 2007a. Numerical implementation of the variational formulation for quasi-static brittle fracture. Interfaces Free Bound. 9 (3), 411–430.
- Bourdin, B., 2007b. The variational formulation of brittle fracture: numerical implementation and extensions. In: IUTAM Symposium on Discretization Methods for Evolving Discontinuities. Springer, pp. 381–393.
- Bourdin, B., Francfort, G., Marigo, J.-J., 2000. Numerical experiments in revisited brittle fracture. J. Mech. Phys. Solids 48 (4), 797–826.
- Bourdin, B., Francfort, G., Marigo, J.-J., 2008. The variational approach to fracture. J. Elasticity 91 (1), 5–148.
- Bragaglia, Mario, Lamastra, Francesca R., Russo, Pietro, Vitiello, Libera, Rinaldi, Marianna, Fabbrocino, Francesco, Nanni, Francesca, 2021a. A comparison of thermally conductive polyamide 6-boron nitride composites produced via additive layer manufacturing and compression molding. Polym. Compos. 42 (6), 2751–2765.
- Bragaglia, Mario, Paleari, Lorenzo, Lamastra, Francesca R., Puglia, Debora, Fabbrocino, Francesco, Nanni, Francesca, 2021b. Graphene nanoplatelet, multiwall carbon nanotube, and hybrid multiwall carbon nanotube-graphene nanoplatelet epoxy nanocomposites as strain sensing coatings. J. Reinf. Plast. Compos. 40 (17–18), 632–643.
- Caporale, A., Luciano, R., Sacco, E., 2006. Micromechanical analysis of interfacial debonding in unidirectional fiber-reinforced composites. Comput. Struct. 84, 2200–2211.
- Cauchy, Augustin-Louis, 1828. Sur l'équilibre et le mouvement d'un système de points matériels sollicités par des forces d'attraction ou de répulsion mutuelle. Exerc. Math. 3 (1822), 1827.
- Ciallella, Alessandro, Giorgio, Ivan, Barchiesi, Emilio, Alaimo, Gianluca, Cattenone, Alberto, Smaniotto, Benjamin, Vintache, Antoine, D'Annibale, Francesco, dell'Isola, Francesco, Hild, François, et al., 2023. A 3D pantographic metamaterial behaving as a mechanical shield: experimental and numerical evidence. Mater. Des. 112554.
- Contrafatto, L., Cuomo, M., Fazio, F., 2012. An enriched finite element for crack opening and rebar slip in reinforced concrete members. Int. J. Fract. 178 (1–2), 33–50.
- Contrafatto, L., Cuomo, M., Gazzo, S., 2016a. A concrete homogenisation technique at meso-scale level accounting for damaging behaviour of cement paste and aggregates. Comput. Struct. 173. 1–18.
- Contrafatto, L., Cuomo, M., Greco, L., 2016b. Meso-scale simulation of concrete multiaxial behaviour. Eur. J. Environ. Civ. Eng. 1–16.
- D'Ambra, Claudio, Lignola, Gian Piero, Prota, Andrea, Fabbrocino, Francesco, Sacco, Elio, 2019. FRCM strengthening of clay brick walls for out of plane loads. Composites B 174, 107050.
- Del Piero, G., Lancioni, G., March, R., 2007. A variational model for fracture mechanics: numerical experiments. J. Mech. Phys. Solids 55 (12), 2513–2537.
- dell'Isola, F., Giorgio, I., Andreaus, U., 2015. Elastic pantographic 2D lattices: a numerical analysis on static response and wave propagation. Proc. Est. Acad. Sci. 64 (3), 219–225.
- dell'Isola, F., Giorgio, I., Pawlikowski, M., Rizzi, N., 2016. Large deformations of planar extensible beams and pantographic lattices: heuristic homogenization, experimental and numerical examples of equilibrium. Proc. R. Soc. Lond. Ser. A Math. Phys. Eng. Sci. 472 (2185), 20150790.
- dell'Isola, Francesco, Guarascio, Massimo, Hutter, Kolumban, 2000. A variational approach for the deformation of a saturated porous solid. a second-gradient theory extending terzaghi's effective stress principle. Arch. Appl. Mech. 70 (5), 323–337.
- Dharmawardhana, C.C., Misra, A., Ching, Wai-Yim, 2014. Quantum mechanical metric for internal cohesion in cement crystals. Sci. Rep. 4 (1), 7332.
- Erden Yildizdag, M., Placidi, Luca, Turco, Emilio, 2023. Modeling and numerical investigation of damage behavior in pantographic layers using a hemivariational formulation adapted for a hencky-type discrete model. Contin. Mech. Thermodyn. 35 (4), 1481–1494.
- Everstine, G.C., Pipkin, A.C., 1973. Boundary layers in fiber-reinforced materials. J. Appl. Mech. 40, 518–522.
- Fabbrocino, F., Carpentieri, G., 2017. Three-dimensional modeling of the wave dynamics of tensegrity lattices. Compos. Struct. 173, 9–16.
- Fabbrocino, F., Farina, I., 2017. Loading noise effects on the system identification of composite structures by dynamic tests with vibrodyne. Composites B 115, 376–383.
- Francfort, G., Marigo, J.-J., 1998. Revisiting brittle fracture as an energy minimization problem. J. Mech. Phys. Solids 46 (8), 1319–1342.

- Gawin, D., Alonso, C., Andrade, C., Majorana, C.E., Pesavento, Francesco, 2005a. Effect of damage on permeability and hygro-thermal\r\nbehaviour of HPCs at elevated temperatures: Part 1. Experimental results. Comput. Concr. 2 (3), 189–202.
- Gawin, D., Majorana, C.E., Pesavento, Francesco, Schrelfer, B.A., 2005b. Effect of damage on permeability and hygro-thermal\r\nbehaviour of HPCs at elevated temperatures: Part 2. Numerical analysis. Comput. Concr. 2 (3), 203–214.
- Gawin, D., Majorana, C.E., Schrefler, B.A., 1999. Numerical analysis of hygro-thermal behaviour and damage of concrete at high temperature. Mech. Cohes.-Frictional Mater. 4 (1), 37–74.
- Giorgio, Ivan, Andreaus, Ugo, dell'Isola, Francesco, Lekszycki, Tomasz, 2017. Viscous second gradient porous materials for bones reconstructed with bio-resorbable grafts. Extreme Mech. Lett. 13, 141–147.
- Giorgio, Ivan, Andreaus, Ugo, Scerrato, Daria, dell'Isola, Francesco, 2016. A visco-poroelastic model of functional adaptation in bones reconstructed with bio-resorbable materials. Biomech. Model. Mechanobiol. 15 (5), 1325–1343.
- Giorgio, Ivan, Ciallella, Alessandro, Scerrato, Daria, 2020a. A study about the impact of the topological arrangement of fibers on fiber-reinforced composites: some guidelines aiming at the development of new ultra-stiff and ultra-soft metamaterials. Int. J. Solids Struct. 203, 73–83.
- Giorgio, Ivan, Dell'Isola, Francesco, Misra, Anil, 2020b. Chirality in 2D cosserat media related to stretch-micro-rotation coupling with links to granular micromechanics. Int. J. Solids Struct. 202, 28–38.
- Grande, Ernesto, Milani, Gabriele, Formisano, Antonio, Ghiassi, Bahman, Fabbrocino, Francesco, 2020. Bond behaviour of FRP strengthening applied on curved masonry substrates: numerical study. Int. J. Mason. Res. Innov. 5 (3), 303–320.
- Greco, L., Cuomo, M., 2013. B-spline interpolation of Kirchhoff-Love space rods. Comput. Methods Appl. Mech. Engrg. 256, 251–269.
- Greco, L., Cuomo, M., 2014. An implicit G1 multi patch B-spline interpolation for Kirchhoff-Love space rod. Comput. Methods Appl. Mech. Engrg. 269, 173–197.
- Greco, Fabrizio, Leonetti, Lorenzo, Luciano, Raimondo, Trovalusci, Patrizia, 2017.
 Multiscale failure analysis of periodic masonry structures with traditional and fiber-reinforced mortar joints. Composites B 118, 75–95.
- Grimaldi, Antonio, Luciano, Raimondo, 2000. Tensile stiffness and strength of fiber-reinforced concrete. J. Mech. Phys. Solids 48 (9), 1987–2008.
- Hu, M.Z., Kolsky, H., Pipkin, A.C., 1985. Bending theory for fiber-reinforced beams. J. Compos. Mater 235–249.
- Khoury, G.A., Majorana, C.E., Pesavento, F., Schrefler, B.A., 2002. Modelling of heated concrete. Mag. Concr. Res. 54 (2), 77–101.
- Lancioni, G., Royer-Carfagni, G., 2009. The variational approach to fracture mechanics. a practical application to the french panthéon in Paris. J. Elasticity 95 (1), 1–30.
- Li, T., Marigo, J.-J., Guilbaud, D., Potapov, S., 2016. Gradient damage modeling of brittle fracture in an explicit dynamics context. Internat. J. Numer. Methods Engrg. 108 (11), 1381–1405.
- Majorana, Carmelo E., Salomoni, Valentina, Schrefler, Bernhard A., 1998. Hygrothermal and mechanical model of concrete at high temperature. Mater. Struct. 31, 378–386.
- Maksimov, Valerii, Barchiesi, Emilio, Misra, Anil, Placidi, Luca, Timofeev, Dmitry, 2021.
 Two-dimensional analysis of size effects in strain-gradient granular solids with damage-induced anisotropy evolution. J. Eng. Mech. 147 (11), 04021098.
- Mancusi, Geminiano, Fabbrocino, Francesco, Feo, Luciano, Fraternali, Fernando, 2017.
 Size effect and dynamic properties of 2D lattice materials. Composites B 112, 235–242.
- Marigo, Jean-Jacques, 1989. Constitutive relations in plasticity, damage and fracture mechanics based on a work property. Nucl. Eng. Des. 114 (3), 249–272.
- Misra, Anil, Ching, W.Y., 2013. Theoretical nonlinear response of complex single crystal under multi-axial tensile loading. Sci. Rep. 3 (1), 1488.
- Misra, Anil, Placidi, Luca, dell'Isola, Francesco, Barchiesi, Emilio, 2021. Identification of a geometrically nonlinear micromorphic continuum via granular micromechanics. Z. Angew. Math. Phys. 72 (4), 1–21.
- Misra, A., Poorsolhjouy, P., 2015. Granular micromechanics model for damage and plasticity of cementitious materials based upon thermomechanics. Math. Mech. Solids 1081286515576821.
- Misra, A., Singh, V., 2015. Thermomechanics-based nonlinear rate-dependent coupled damage-plasticity granular micromechanics model. Contin. Mech. Thermodyn. 27 (4–5), 787.
- Navier, Claude-Louis-Marie-Henri, 1827. Sur les lois de l'equilibre et du mouvement des corps solides elastiques.
- Placidi, Luca, Barchiesi, Emilio, 2018. Energy approach to brittle fracture in strain-gradient modelling. Proc. R. Soc. Lond. Ser. A Math. Phys. Eng. Sci. 474 (2210), 20170878
- Placidi, Luca, Barchiesi, Emilio, Dell'Isola, Francesco, Maksimov, Valerii, Misra, Anil, Rezaei, Nasrin, Scrofani, Angelo, Timofeev, Dmitry, 2022. On a hemi-variational formulation for a 2D elasto-plastic-damage strain gradient solid with granular microstructure. Math. Eng. 5, 1–24.
- Placidi, Luca, Barchiesi, Emilio, Misra, Anil, Timofeev, Dmitry, 2021. Micromechanics-based elasto-plastic-damage energy formulation for strain gradient solids with granular microstructure. Contin. Mech. Thermodyn. 33, 2213–2241.
- Poorsolhjouy, Payam, Misra, Anil, 2017. Effect of intermediate principal stress and loading-path on failure of cementitious materials using granular micromechanics. Int. J. Solids Struct. 108, 139–152.
- Qingfu, Li, Wei, Guo, Yihang, Kuang, 2020. Parameter calculation and verification of concrete plastic damage model of ABAQUS. IOP Conf. Ser.: Mater. Sci. Eng. 012036.

- Ramaglia, Giancarlo, Lignola, Gian Piero, Fabbrocino, Francesco, Prota, Andrea, 2018.

 Numerical investigation of masonry strengthened with composites. Polymers 10 (3), 334.
- Reddy, B., 2011a. The role of dissipation and defect energy in variational formulations of problems in strain-gradient plasticity. Part 1: polycrystalline plasticity. Contin. Mech. Thermodyn. 23, 527–549.
- Reddy, B., 2011b. The role of dissipation and defect energy in variational formulations of problems in strain-gradient plasticity. Part 2: Single-crystal plasticity. Contin. Mech. Thermodyn. 23, 527–549.
- Scerrato, D., Giorgio, I., Della Corte, A., Madeo, A., Limam, A., 2015. A micro-structural model for dissipation phenomena in the concrete. Int. J. Numer. Anal. Methods Geomech
- Scerrato, Daria, Giorgio, Ivan, Madeo, Angela, Limam, Ali, Darve, Felix, 2014. A simple non-linear model for internal friction in modified concrete. Internat. J. Engrg. Sci. 80, 136–152.
- Schrefler, B.A., Brunello, Pierfrancesco, Gawin, D., Majorana, C.E., Pesavento, Francesco, 2002a. Concrete at high temperature with application to tunnel fire. Comput. Mech. 29, 43–51.

- Schrefler, Bernhard A., Majorana, Carmelo E., Khoury, Gabriel A., Gawin, Dariusz, 2002b. Thermo-hydro-mechanical modelling of high performance concrete at high temperatures. Eng. Comput. 19 (7), 787–819.
- Simulia, 2014. Abaqus Analysis User's Guide. Abaqus, pp. 25-52.
- Timofeev, Dmitry, Barchiesi, Emilio, Misra, Anil, Placidi, Luca, 2021. Hemivariational continuum approach for granular solids with damage-induced anisotropy evolution. Math. Mech. Solids 26 (5), 738–770.
- Turco, E., dell'Isola, F., Rizzi, N.L., Grygoruk, R., Müller, W.H., Liebold, C., 2016.
 Fiber rupture in sheared planar pantographic sheets: Numerical and experimental evidence. Mech. Res. Commun. 76, 86–90.
- UNI/CT 009, 2022. Hardened concrete test part 1: Shape, dimensions and other requirements for specimens and formwork, UNI. pp. 1-9.
- UNI/CT 021/SC 04 UNI/CT 021, UNI/CT 021/GL 03, 2015. Test method for concrete with metallic fibers measurement of bending tensile strength [limit of proportionality (LOP), residual strength], UNI. pp. 8–12.